

## Highlights

- This review covers the synthesis, characterization, and applications in electrochemical sensors of 2D layered pnictogens.
- Phosphorene is the most popular 2D layered pnictogen for electrochemical sensing.
- Bismuthene and antimonene are gaining interest in the design of electrochemical sensors.
- Arsenene is not an attractive material for biosensing due to its acute toxicity.

# Phosphorene and other layered pnictogens as a new source of 2D materials for electrochemical sensors

María A. Tapia<sup>1</sup>, Rui Gusmão<sup>2\*</sup>, Núria Serrano<sup>1,3\*</sup>, Zdeněk Sofer<sup>2</sup>, Cristina Ariño<sup>1,3</sup>, José Manuel Díaz-Cruz<sup>1,3</sup>, Miquel Esteban<sup>1,3</sup>

<sup>1</sup>Department of Chemical Engineering and Analytical Chemistry, University of Barcelona, Martí i Franquès 1-11, 08028-Barcelona, Spain, e-mail: nuria.serrano@ub.edu

<sup>2</sup>Department of Inorganic Chemistry, University of Chemistry and Technology Prague, Technická 5, 166 28 Prague 6, Czech Republic, e-mail: rui.gusmao@vscht.cz

<sup>3</sup>Water Research Institute (IdRA), University of Barcelona, Martí i Franquès 1-11, 08028-Barcelona, Spain

\*Corresponding author to whom correspondence should be addressed.

## Abstract

Following the great success of graphene as a versatile 2D nanomaterial for the design of electrochemical sensors, this review focuses on the synthesis, characterization, and electrochemical sensing applications of alternative 2D layered structures produced with elements of group VA, also known as “pnictogens.” Among these, phosphorene nanosheets generated from black phosphorous (BP) is by far the most popular 2D layered pnictogen; however, bismuthene and antimonene are also gaining interest in the design of electrochemical sensors. A perspective is given to the properties of the various layered pnictogens and factors affecting their stability, which also influence their sensing abilities. Examples using arsenene are still relatively sparse as this is not an attractive material for biosensing due to its acute toxicity. Tables with the most meaningful information from the available literature are presented.

**Keywords:** Pnictogens; Black phosphorus; Phosphorene; Bismuthene; Antimonene; Arsenene; 2D materials; Electrochemical sensing applications; Electrochemical sensors; Gas sensing

## 1. Introduction

2D layered materials have aroused great attention in the last decades due to their exceptional physical properties and outstanding features, such as large surface area, morphology tunability, great mobility, and the possibility to change their surface properties, which make them feasible to be applied in optoelectronics, catalysis, energy storage, and sensors [1]. Graphene is nowadays the most renowned 2D layered material, but there are other elements of group VA (also called “pnictogens” or the “nitrogen” group) that can also adopt a layered structure. These elements are named in an analogous way to graphene, i.e., phosphorene, bismuthene, antimonene, and arsenene. The main difference among these is that phosphorene and arsenene can have an orthorhombic crystal structure, whereas the rest have the same rhombohedral structure as graphene, although graphene has truly a single-atom thick monolayer.

Accelerated by interest from the scientific community, the class of 2D layered nanomaterials continues to grow. The post-graphene 2D monoelemental material black phosphorus (BP) has gained significant interest recently due to its outstanding physical and chemical properties [2]. BP is a newcomer 2D monoelemental P layered material, and other layered materials from the pnictogens group (N family or group 15 or VA) are now also emerging. These consist of the elements nitrogen, phosphorus, arsenic, antimony, bismuth, and synthetic moscovium. Considering merely the layered allotrope single-elements from Group VA, orthorhombic BP is semi-conductive, with a large in-plane anisotropic magnitude of physical properties, and

tunable direct bandgap [3]. Heavier elements in the pnictogen group are semimetals and, in monolayers, also semiconductors with layered rhombohedral structures (grey or  $\beta$ -arsenic, -antimony, and -bismuth). Arsenic exists also in metastable allotrope with true van der Waals structure similar to BP, black arsenic [1].

Compared to orthorhombic phases, rhombohedral phases also exhibit covalent interactions between individual layers and the intensity of these interactions increases with the atomic number of the element (**Figure 1**). However, the most significant bottleneck of BP and its monolayer phosphorene to widespread applications is their intrinsic instability due to rapid oxidation coupled with light- and oxygen-induced degradation under ambient humidity conditions [2]. The degradation of the heavier 2D pnictogen has been noted not to be as severe as in the case of BP, but not immune to this phenomenon. Several strategies have been proposed to address this critical issue such as protective functionalization and van der Waals heterostructures. Their chemistry shifts from non-metal (P) to metalloids (As and Sb) to post-transitional metal (Bi). Besides the successful application of 2D pnictogens as sensing platforms, they have also been reported as a potential alternative nanomaterial in batteries, transistors, photodetectors, and photovoltaic cells [1].

The high interest in pnictogens-based sensors can be traced back to deposited film electrodes as mercury substitutes for electrode material. Since their introduction, bismuth film electrodes (BiFE) have become an attractive platform for electroanalytical purposes, being environmentally friendly and offering the features closest to mercury [4]. Similarly, antimony film electrodes (SbFE) feature interesting characteristics such as favorably negative overvoltage of hydrogen evolution, wide operational potential window, convenient operation in acidic solutions of pH 2 or lower, and a minimal stripping signal for antimony itself under some conditions. Thus, it is only natural that as layered pnictogens become more available, an increasing number of applications of these materials as sensing platforms are realized.

Nevertheless, and despite their interesting features, these alternative 2D monoelemental layered materials are still applied less for sensing than graphene [5]. In this review, we summarize the most relevant properties of layered pnictogens, the top-down and bottom-up methods for the fabrication of 2D pnictogens, functionalization strategies, characterization, and, especially, their most recent applications for electrochemical sensing from 2017 onwards.

## **2. Synthesis and characterization of 2D layered pnictogen materials**

Unanimity has not been reached as to how to designate a monolayer of layered pnictogens. The majority of the literature usually refer to a few-layer BP as phosphorene, with “-ene” used as a suffix for BP and the remaining layered pnictogens. This is in close relation to graphene and for the prestige its name association brings. Nevertheless, this does not fully support IUPAC chemical terminology as the “ene” suffix is assigned to systems with double bonds [1]. In this review, elements from the pnictogen group will hereafter be referred to as “pnictogens” and the suffix “-ene” will be used for the sake of simplicity when referring to exfoliated and few-layer materials.

### ***2.1 Synthesis, properties, and exfoliation***

For BP, there are several synthetic routes: the original method, first reported in 1914, involves the high-pressure conversion of white or red phosphorus. High-pressure conversion proceeds at pressure higher than 6 GPa and temperature above 200°C. Later, the formation of BP from red phosphorus in the environment of mercury or bismuth at high temperature was reported. This synthesis led to the contamination of formed BP by catalytic metals. Currently, the most commonly used method involves vapor crystal growth using Si and SnI<sub>4</sub> mineralizer in a sealed quartz ampoule [2]. While the high pressure method produces highly compact nanocrystallite BP and large crystals are formed only by slow cooling, vapor-grown BP usually produces very nicely defined pellets of mm-wide crystals (**Figure 2A**). However, this method led to the

incorporation of tin and iodine in the crystals. Grey or rhombohedral arsenic, antimony, and bismuth occur naturally; thus, these are the most commonly used phases in most works. Black or orthorhombic arsenic can be synthesized from amorphous arsenic using mercury as catalyst by adapting the BP vapor growth method [6].

BP is narrow bandgap semiconductor with intrinsic p-type conductivity and high carrier mobility. The electronic structure is strongly dependent on the number of layers and, compared to bulk BP with bandgap about 0.4 eV, monolayer phosphorene has a bandgap of around 2 eV. BP is highly reactive and its degradation is induced by the presence of oxygen; hence, this creates significant limitations in its applications due to surface formation of phosphorus oxides and, ultimately, phosphorus acid.

Layered pnictogens' degradation in ambient conditions—particularly for BP—has been a significant challenge for researchers attempting to find proper ways of passivation or encapsulation when applying BP to different devices. The layered puckered structure with a free pair of electrons and hydrophilic surface allow the decomposition of BP to phosphoric acid species in the presence of  $O_2$ ,  $H_2O$ , or even by photo-oxidation. Although not exclusive to BP, to some extent, partial oxidation of the heavier 2D pnictogens is also verified in a considerable portion of works [1]. The most common strategies for new sensing assembling strategies involve the integration of BP in van der Waals heterostructures with other 2D layered materials [7] as an alternative, organic covalent and non-covalent functionalization for passivation.

Liquid-phase exfoliation (LPE) has been successfully employed to generate few-layer 2D pnictogens on a large scale (**Figure 2B**). Monolayer or few-layer 2D pnictogens have been obtained experimentally by top-down methods of bulk pnictogen (e.g., liquid-phase exfoliation) or bottom-up methods (e.g., epitaxial growth). High-yield preparation by top-down methods of high-quality, few-layer 2D pnictogens has been reported for mechanical and liquid-phase exfoliation (LPE) methods [8]. Different LPE of layered pnictogens, such as high shear

rate (ultrasonic-assisted and electrochemical) have been reported. Shear exfoliation is the most commonly used technique and allows for higher scalability of exfoliated 2D pnictogens. Electrochemical exfoliation of BP to phosphorene [9] and the heavier grey pnictogen to few-layer 2D pnictogen [10,11] has been reported in both aqueous and organic solvent, using anodic, cathodic, or bipolar current modes.

The production, manipulation, application, and disposal of 2D pnictogens also introduce the need to control the impacts of their presence in the environment and the effects on users. The biological effects for regulatory assessment of 2D pnictogens are still mostly unidentified and should not be ignored. While acute exposure can assess the immediate and early impact, chronic exposure over more extended periods may reveal long-term biological effects of 2D pnictogens both for *in vitro* and *in vivo* systems [12]. Research points to the fact that the degree of exfoliation, size, and oxidation all have a crucial role in the toxicity of the materials. It seems that the toxicity of 2D pnictogens decreases along with the group, with bismuthene considered the least toxic, in accordance with the clinical biosafety of bismuth-based drugs [13]. Predictably, arsenene or exfoliated 2D arsenic was found to be highly toxic and, thus, the least attractive 2D pnictogen to work with to develop sensing devices.

## **2.2 Characterization of 2D layered pnictogens**

Due to possible sample inhomogeneity, single measurements at some regions of a sample can be strongly misleading. X-ray photoelectronspectroscopy (XPS) is useful to obtain information on the chemical composition of bulk and exfoliated materials, evaluate of their stability, and detect the presence of oxidized groups, which also have a significant influence on electrochemical sensing (**Figure 2C**). The deconvolution of Sb 3d is probably the most intricate of the 2D pnictogens due to doublet separation for Sb 3d<sub>5/2</sub> and 3d<sub>3/2</sub> overlaps with the O 1s spectrum. One useful approach is to fit and constrain the Sb 3d<sub>5/2</sub> and 3d<sub>3/2</sub> peaks as a criterion (with  $\Delta = 9.39$  eV). The remaining area in the 3d<sub>5/2</sub> area should be related to the O 1s signal(s).

XPS has some limitations considering that useful information can only be obtained from the top atomic layers of the materials, which compromise reliability for the entire mass of highly heterogeneous materials. Besides, because small changes in oxidation states typically generate overlapping signals, analysis of a particular element can only provide a rough estimation of its oxidation states.

Scanning electron microscopy (SEM) and transmission electron microscopy (TEM) are powerful imaging tools to characterize 2D pnictogens. High-resolution TEM (HRTEM) can reach atomic resolution with clear visualization of the lattice, shape, and estimation of lateral size of 2D pnictogens (**Figure 2D**). Combined with EDX spectra and mapping of elements, it becomes a very useful option to confirm elements and their abundance in the exfoliated 2D pnictogen materials. Atomic force microscopy (AFM) is probably the best technique available to identify the structure of 2D pnictogen sheets and to estimate the number of layers; it is also useful for controlling the morphology in the case of material degradation (**Figure 2E**). Dynamic light scattering (DLS) measurements allow for a quick survey of particle sizes, although results relate to the hydrodynamic diameter of nanomaterials, usually optimized for spherical particles, thus the application to flat layered material might be considered much less reliable.

Raman spectroscopy of 2D pnictogens allows examination of the crystal structure, with the spectra showing thickness dependent and being also indicative of oxidation of materials and is especially useful when correlated with AFM measurements (**Figure 2F**). Another example is the structural difference between g-As and b-As, belonging to R-3m and Cmca space groups, respectively. Examination by Raman spectroscopy reveals very different active lattice vibration modes as seen in **Figure 2G**.

Relative to their electrochemistry and as observed for graphene, 2D pnictogens are reported to have fast heterogeneous transfer at the edge planes and slow transfer at the basal plane for many electroactive molecules. This is especially noticeable for the highly anisotropic BP, for which the electron-transfer rates differ at the basal and edge planes as demonstrated for AA

and DP (**Figure 2H**), thus affecting its sensing performance [17]. An increasing activity trend of the basal plane with higher atomic number was observed and attributed to the decreasing degree of anisotropy of the material [18]. Relative to their inherent electrochemistry, BP has a highly pronounced and irreversible oxidation peak *ca.* + 0.6 V (vs. AgCl), corresponding to the oxidation of  $P^0$  to  $P^{5+}$  [19], thus being an almost irresponsive post-oxidation process, which might limit its application to analytes having electrochemical processes at similar or higher potentials. The heavier 2D pnictogens have more stable electrochemistry over a wider potential range at neutral pH [20]. While g-Bi is oxidized to  $Bi^{3+}$ , for g-As and g-Sb the observed processes were oxidation to pnictogen $^{3+}$  and pnictogen $^{5+}$ , with the reverse reduction to pnictogen $^{3+}$  and elemental pnictogen $^0$  [18].

Finally, for BP it has been observed that BP synthetic routes, such as high-pressure conversion ( $BP^{hp}$ ) and vapor phase growth ( $BP^{vg}$ ), may not only introduce or retain different metal impurities but additionally influence its exfoliation process [19,21].  $BP^{vg}$  consisting of large well-developed crystals obtained by vapor growth methods and containing trace amounts of Sn is easily delaminated and exfoliated. On the other hand, the nanocrystalline  $BP^{hp}$  method could not be extensively exfoliated by shear force. Starting material BP crystallinity therefore influenced its shear-exfoliated counterpart BP's surface chemistry, oxidation, and electrochemical performance, with comparatively better results being obtained for  $BP^{vg}$ . For  $BP^{vg}$ , however, traces of Sn or I might be found, both  $BP^{hp}$  and  $BP^{vg}$  may retain the metallic impurity from the precursor, such as Fe or Ni, which influences the voltammetric and sensing performance of BP. For b-As, levels of Hg up to 5% wt. have been observed as necessary for the stabilization of orthorhombic As [6]. From a survey of the literature and commercial providers, the most commonly used BP in most works has been  $BP^{vg}$ , which has a market price within the order of 500 euros/g. For heavier 2D pnictogens, b-As prices are around 500 euros for a crystal (weight unspecified), while grey 2D pnictogens are most stable allotropes and are broadly commercially available.

### 3. Phosphorene-based electrochemical sensors

Phosphorene, a single atomic layer of BP, has attracted significant interest over the last decade, becoming the most recognized and experimentally studied 2D pnictogen material for electrochemical sensing applications. **Tables 1** and **2** provide an overview of recent advances (from 2017 until December 2020) in electrochemical sensing achieved with BP.

#### 3.1 Phosphorene -based sensors for gas sensing electrochemical applications

Different techniques have been reported for the synthesis of BP. As mentioned previously, liquid-phase exfoliation and mechanical exfoliation are currently the most used techniques. Nevertheless, Phan *et al.* reported the synthesis of several gram-scale BP powder using the high-energy ball milling technique [23].

BP has a great affinity for water molecules and has been applied to the development of humidity sensors based on different transduction principles [22–27]. In addition, composites of BP with other materials, such as indium oxide, CuO/pyrrole-BP nanocomposite, anthraquinone nanowire (AQNW), and chemically passivated phosphorene (CPP) with porous triazine-based two-dimensional polymer (T-2DP) or noble metals, have been applied to the detection of gases such as NO<sub>2</sub> or H<sub>2</sub> [28–34]. **Table 1** summarizes and compares the main characteristics of different BP-based sensors applied to gas sensing. As it can be seen, the field-effect transistor (FET) is one of the most commonly used transducers modified by the dry transfer technique. It should also be noted that Al<sub>2</sub>O<sub>3</sub>, or Nafion, can be used as a passivation layer to improve BP stability against degradation. In this respect and according to Walia *et al.* who investigated the effects of key environmental factors on BP degradation—humidity, light, and temperature—photo-oxidation is the main cause of BP deterioration [26]. Further works studied the influence of discrete wavelengths ranging from UV to IR on the degradation of BP, revealing that the UV component of the spectrum is mainly responsible for the degradation of BP in ambient

conditions [67]. Thus, BP manipulation in a UV-deficient atmosphere should be enough to protect it against photo-oxidation.

As an example of the devices summarized in **Table 1**, **Figure 3** shows a sensor that combines the adsorption of water molecules by BP nanosheets with a quartz crystal microbalance (QCM) [22]. BP-based QCM sensors display a well-defined logarithmic frequency response to humidity and the sensor sensitivity is closely linked to the amount of BP nanosheets used in the deposition process. Another strategy for humidity sensors is based on the drop-casting of BP on the sensing slots of a substrate-integrated waveguides (SIWs) resonators, whose sensitivity noticeably increases compared with that achieved by the sensor without a BP-sensitive layer [24]. Another humidity sensor approach [25] is based on the integration of BP in an FET fully encapsulated by a layer of Al<sub>2</sub>O<sub>3</sub>. In this study, after being stored in air for more than a week, the encapsulated BP sensor was found to have higher ambient stability with no appreciable degradation in sensing response. Moreover, BP can be combined with silver nanoparticles in an ink that is used to fabricate printed electrodes as humidity sensors [27]. On the other hand, composites of BP with In<sub>2</sub>O<sub>3</sub> can be applied to the selective sensing of NO<sub>2</sub> by means of measurements of resistance. In addition, it is demonstrated that the introduction of In<sub>2</sub>O<sub>3</sub> remarkably improved the BP environmental stability [28]. Another BP-based sensor approach for gas sensing consists of attaching floating BP flakes on the top of the electrode in order to make both sides available for adsorption [29]. Finally, the incorporation of noble metals like Au or Pt to BP nanosheets can remarkably enhance their sensitivity to H<sub>2</sub> [33,34]. **Figure 4** illustrates the fabrication of these sensing devices [34]. BP flakes were mechanically exfoliated from bulk BP crystals using a transparent transfer film in an Ar-filled glove box. Then, the flakes were transferred by dry transfer technique onto an FET pattern containing SiO<sub>2</sub>/p-Si substrate as the back gate as well as two Ti/Au layers constituting the source and the drain. The transferred BP flakes were coated with Pt NPs prior to the application of a protective poly(methylmethacrylate) (PMMA) layer, which is hydrophobic and permeable to hydrogen. In

this way, when H<sub>2</sub> molecules cross the PMMA barrier and are adsorbed onto Pt NPs, they dissociate to form atomic hydrogen, which transfers electrons to the hole carriers in BP exhibiting intrinsic p-type characteristics and results in a current reduction that is used for hydrogen sensing.

### **3.2 Phosphorene -based sensors for non-gas sensing electrochemical applications**

BP is not only used in the design of gas sensors; indeed, the sensing applications of BP in liquid samples are considerably more numerous and diverse as shown in **Table 2** [35–66]. Some sensing devices, including BP, are based on an FET configuration and current–potential measurements. This is the case for sensors for metal ions such as Hg(II) [35], As(III)/(V) [36], Pb(II) [38], or Ag(I) [39]. **Figure 5** shows the structure of the BP sensor for As(III)-ions where an exfoliated BP film is transferred onto interdigitated Au electrodes in the sensitive part of the FET and then sputtered with Au nanoparticles functionalized with dithiothreitol (DTT) molecules to take advantage of their affinity for As(III)-ions [36]. The signals obtained are also shown in **Figure 5**. In Ref. [37], BP flakes were incorporated into a flexible substrate of poly(ethylene terephthalate) (PET) and functionalized with different ionophores for the multiplexed detection of Hg(II), Cd(II), Pb(II), and Na(I) in sweat and tap water samples. In Ref. [53], the deposition of anti-human IgG-conjugated gold nanoparticles on the surface of the Al<sub>2</sub>O<sub>3</sub> dielectric layer of a BP-based FET produces a sensor to detect human immunoglobulin G (IgG). Other sensing devices use BP as a substrate for different nanocomposites, including nanoparticles and selective molecules, and focus on measurements by impedance spectroscopy (EIS) or electrochemiluminescence (ECL). Although such a strategy is mostly used to detect cells, cell fragments, and proteins related to cancer and other diseases in human serum [63–65], it has been also applied to the highly sensitive detection of Pb(II)-ions in tap and lake water samples [66]. As an example, **Figure 6** shows the operating principle of the sensor reported in [65] for the detection of lysozyme (Lyz) using a Lyz aptamer. BP quantum

dots (BPQDs) are protected against oxidation, being embedded in a styrene/acrylamide (St-AAm) copolymer to form nanospheres, denoted in the scheme as BSAN. In this form, they enhance the ECL of  $\text{Ru}(\text{bpy})_3^{2+}$ , acting as a coreactant. As seen in **Figure 6**, a Lyz aptamer is linked to a gold electrode through an S-Au bond. BSAN is connected with DNA through the amino group on the polymer film and then BSAN/DNA immobilizes onto the electrode through DNA hybridization. The connected BSAN reacts with  $\text{Ru}(\text{bpy})_3^{2+}$  to generate a strong ECL signal. When the sensor is incubated in Lyz solution, the specific interaction between Lyz and aptamer releases BSAN/DNA from the electrode surface, which causes a decrease of ECL signal.

Nevertheless, most BP sensing applications are based on different modalities of amperometry and voltammetry (cyclic voltammetry, CV; differential pulse voltammetry, DPV; square wave voltammetry, SWV; amperometry; chronoamperometry, CA) [41–52]. Many of these modalities take advantage of the electrocatalytic properties of BP to modify glassy carbon electrodes (GCE) together with other components, or to form composites of enhanced stability either with ZnO nanoparticles for the detection of  $\text{H}_2\text{O}_2$  [43], or with ionic liquid (IL) and poly(diallyldimethylammonium chloride) (PDDA) [40], or with the conducting polymer poly(3,4-ethylenedioxythiophene)-poly(styrenesulfonate) (PEDOT:PSS) [41,42,44]. In these last two cases, the resultant nanocomposites facilitate the immobilization of hemoglobin [40–42] and hemin [44], achieving an excellent electrocatalytic response toward  $\text{NaNO}_2$ , trichloroacetic acid (TCA),  $\text{H}_2\text{O}_2$ , and  $\text{O}_2$ , which is essential in numerous biochemical studies [40–42, 44]. In Ref. [52], a similar incorporation of BP with PEDOT:PSS onto a GCE is used to determine the flavonoid glycoside rutin in rutin tablet samples. Other remarkable applications include detection of the biomarker  $\alpha$ -hydroxybutyrate (AHB) [45] or the drug clenbuterol [49,50] in serum and other biological samples, the detection of the plastic residue bisphenol A in water and urine samples [46,47], or the sensing of the fungal toxin achratoxin A in grape juice and beer samples [48]. In order to illustrate the shape and evolution of the signals obtained with these sensors, **Figure 7** shows characteristic amperograms measured with the sensor of  $\text{H}_2\text{O}_2$

described in [43] while **Figure 8** shows characteristic voltammograms obtained with the sensor of ochratoxin A (OTA) described in [48]. Although most of the BP-based sensors are designed for static measurements, there are also flow designs such as the microfluidic system proposed in [51] for the detection of the biotoxin okadaic acid (OA) in mussel samples using a screen-printed carbon electrode (SPCE) modified by phosphorene-gold nanocomposite onto which an aptamer specific to OA was immobilized.

#### **4. Electrochemical sensors based on antimonene, bismuthene, and arsenene**

Several first-principles studies have been published comparing the few articles that experimentally evaluate the electrochemical sensing response feasibility of 2D pnictogens beyond phosphorene such as antimonene, bismuthene, and arsenene. These experimental studies of the heavier elements of the pnictogen group are summarized in **Table 3**.

In these studies, different exfoliation techniques of layered pnictogens are used, with shear force exfoliation being the most common. Particularly, Gusmão *et al.* [20,68] reported a shear force mixing procedure to obtain exfoliated nanosheets of rhombohedral layered As, Sb, and Bi without the need for purged media, with a yield (%) of 8.8, 8.2, and 3.9 for Bi<sub>SE</sub>, Sb<sub>SE</sub>, and As<sub>SE</sub>, respectively. Adapting this method, Lazanas *et al.* [73] also reported a shear force liquid-phase exfoliation method for the production of bismuthene in an aqueous surfactant medium (sodium cholate) with a yield of 1.2%. It was found that shear exfoliation generates edges and active sites that provide characteristics of non-inert materials for each pnictogen shear exfoliated. This withholds distinct native oxidation and reduction signals and further induces new activated edges that improve the electrode response and catalytic properties compared to the bulk material [20].

The electrode modification methodology was, in most cases, the drop-casting approach, with the mass of 2D material drop-casted ranging from 2–100 µg depending on the considered

sensor. Most of the drop-casted dispersions were monoelemental. However, Lazanas *et al.* [73] reported the development of a hybrid bismuthene/graphene electrode prepared from a dispersion consisting of a mixture of 2 mg bismuthene and 10 mg graphene in 2 mL DMF. The electrode surface can be also modified with Nafion solution after the modification with 2D materials [73]. The preferred substrates in which the 2D material suspension is drop-casted are based on carbon [20,68,70,73,74] and on gold [6,69,72], being the glassy carbon and the screen-printed carbon or gold electrodes, the most commonly used supports.

Different techniques were used to describe the electrochemical behavior and feasibility of 2D pnictogens as sensing platforms. Specifically, two of the works [20,68] summarized in **Table 3** compare the chemical and morphological characteristics, electrochemical behavior, and sensing response feasibility between the 2D pnictogen materials. In both cases, the best performance was achieved for devices based on shear exfoliated antimonene sensors.

Antimonene is the 2D pnictogen material with the highest degree of exfoliation, forming sheets of few-layer thicknesses and the lowest oxidation-to-bulk ratio as compared to the other pnictogens, which could enhance its performance. The biocompatibility of antimonene with enzyme activity and the strong interaction with DNA suggest its capability for biosensing devices as compared to arsenene, which inhibits enzyme activity [68,69]. Moreover, antimonene quantum dots in conjunction with catalase enzyme also show their suitability as biosensing material for use in clinical diagnosis, being able to determine the concentration of H<sub>2</sub>O<sub>2</sub> in ovarian cancer serum and, therefore, predict the cancer stage [70].

Regarding arsenene, Antonatos *et al.* [6] reported an acetonitrile-assisted exfoliation procedure for black and grey arsenic that forms a stable dispersion for eight days in acetonitrile. Black arsenic presents a more efficient exfoliation procedure than grey arsenic, leading to arsenic nanosheets with a thickness below 3 nm compared to the grey arsenic nanosheets having a thickness of 20–30 nm. Arsenic-based devices demonstrate potential

applications in gas sensing and photothermal absorption. Particularly, black arsenic was more suitable as a volatile organic compounds (VOCs) sensor based on electrochemical impedance spectroscopy (EIS) due to its sensitivity toward five VOCs: methanol, ethanol, isopropanol, acetone, and acetonitrile. As for grey arsenic, it was sensitive to methanol and ethanol [6]. **Figure 9** compares the impedimetric signals obtained by using both 2D nanomaterials. Beladi-Mousavi *et al.* [72], reported a liquid-phase exfoliation procedure to prepare few-layer arsenene nanosheets with controllable sizes assisted by sonication and without any additional surfactant. These 2D As nanosheets were also applied for the development of an impedimetric vapor sensor, which selectively detects acetone and methanol vapors. In both studies [6,72], a frequency dependence of the sensor response (phase shift) was found, allowing the selective detection between individual VOCs.

Bismuthene, another 2D pnictogen material, was used for the modification of voltammetric sensors based entirely on bismuthene [74] or as a hybrid bismuthene/graphene [73] to enhance the properties of conventional bismuth-based electrodes, due to the strongest features of this 2D material [75,76]. In combination with tunable bandgap over a broad range and electronic transport properties makes this material highly attractive for field effect transistors, photodetectors, and sensors [77]. Their analytical performance suggests suitability for the determination of Cd(II) and Pb(II) ions by anodic stripping voltammetry (ASV) at concentration levels of low  $\mu\text{g L}^{-1}$ , being the detection limits of the sensor based entirely on bismuthene, which is about five times lower than those obtained with the hybrid bismuthene/graphene sensor and much lower than those obtained for Pb(II) and Cd(II) on conventional bismuth-based sensors [74]. Both 2D Bi-based sensors were successfully applied for the simultaneous voltammetric determination of trace Pb(II) and Cd(II) in water samples. **Figure 10a** compares the ASV peaks obtained for both heavy metal ions by using carbon screen-printed electrodes (SPCE) modified with bismuth in different ways (Bi nanoparticles, sputtered Bi, Bi films, and shear exfoliated Bi). It can be seen that the electrode modified with

exfoliated bismuth clearly outperforms the others. As a result, really low concentrations of Cd(II) and Pb(II) can be determined as shown by **Figure 10b**, corresponding to the analysis of a certified estuarine water sample by means of the standard addition method.

Furthermore, novel pnictogen nanosheets such as antimonene, arsenene, and bismuthene can be mixed with metal-based nanostructures, resulting in composites that synergistically merge the exceptional properties of both materials. In particular, arsenene combined with gold@silver nanorods exhibits exceptional electrocatalytic ability toward glucose oxidation, being the basis for the development of a nonenzymatic glucose sensor [71].

Finally, as a representative study of the electrochemical sensing performance of the 2D pnictogen materials, we will summarize the work of Mayorga-Martinez *et al.* [68] who explored and compared the biosensing analytical performances of pnictogen materials (phosphorene, antimonene, arsenene, and bismuthene) to detect phenol. They developed enzymatic sensors based on bulk and shear exfoliated pnictogen materials. **Figure 11** illustrates the fabrication and use of these biosensors: first, shear exfoliated pnictogens are generated with a kitchen blender; second, they are deposited by drop-casting onto a glassy carbon electrode; third, the biochemical modifiers (Tyr and Glu) are added; and, finally, the biosensors are applied to the electrochemical detection of phenols. The best performance in terms of linearity, sensitivity, selectivity, and reproducibility was obtained by the antimonene shear exfoliated-based biosensor as compared to the other pnictogen biosensors studied.

So far, few electrochemical sensing studies have been carried out with 2D materials based on elements of the pnictogen group other than phosphorus; however, future applications of sensors and biosensors based on these materials are beginning to actively unfold in a great variety of analytes. These few studies summarized in **Table 3** are just a teaser of wider possibilities in the sensing field.

## **Conclusions**

Efforts to obtain few-layer 2D pnictogens experimentally by top-down methods of bulk pnictogen (e.g., liquid-phase exfoliation) or bottom-up methods (e.g., epitaxial growth) have made this class of materials more accessible and appealing for sensor design. In particular, shear exfoliated 2D structures can be obtained in a relatively easy and cost-effective way from elements' bulk crystals of the pnictogen group as an alternative/complement to carbon-based nanomaterials such as graphene. Given their excellent properties, phosphorene, antimonene, bismuthene, and arsenene can become key structural elements in the design of electrochemical sensors for the detection of a multitude of substances in both gas and solid samples. The biological effect of 2D pnictogens is still mostly unidentified and should not be ignored. Arsenene or exfoliated 2D arsenic was found to be highly toxic, making this the least attractive 2D pnictogen to work with to develop sensing devices. Layered pnictogens can suffer from degradation in ambient conditions, which has been a significant challenge for research with these materials. The organic covalent and non-covalent functionalization for passivation is highly attractive for new sensing device design strategies.

## **Acknowledgments**

This work is supported by the Ministry of Science and Innovation of Spain (Project PID2019-107102RB-C22) and the Generalitat of Catalunya (Project 2017SGR311). M.A.T. would like to thank the Peruvian National Program of Scholarships and Student Loans (PRONABEC) for her Ph.D grant (Beca Presidente de la República -343245). M.A.T. appreciates the support of the Water Research Institute (IdRA) of the University of Barcelona. Financial support from the Ministry of Education Youth and Sports (MEYS) of the Czech Republic (Project GACR No 19-26910X) is also gratefully acknowledged.

**Author contributions**

All authors discussed, commented, and revised the manuscript.

## References

- [1] S. Zhang, S. Guo, Z. Chen, Y. Wang, H. Gao, J. Gómez-Herrero, P. Ares, F. Zamora, Z. Zhu, H. Zeng, Recent progress in 2D group-VA semiconductors: From theory to experiment, *Chem. Soc. Rev.* 47 (2018) 982. <https://doi.org/10.1039/c7cs00125h>.
- [2] R. Gusmão, Z. Sofer, M. Pumera, Black phosphorus rediscovered: from bulk material to monolayers, *Angew. Chemie - Int. Ed.* 56 (2017) 8052. <https://doi.org/10.1002/anie.201610512>.
- [3] A. Hirsch, F. Hauke, Post-graphene 2D chemistry: The emerging field of molybdenum disulfide and black phosphorus functionalization, *Angew. Chemie - Int. Ed.* 57 (2018) 4338. <https://doi.org/10.1002/anie.201708211>.
- [4] N. Serrano, J.M. Díaz-Cruz, C. Ariño, M. Esteban, Antimony- based electrodes for analytical determinations, *TrAC - Trends Anal. Chem.* 77 (2016) 203. <https://doi.org/10.1016/j.trac.2016.01.011>.
- [5] V. Lloret, M.A. Rivero-Crespo, J.A. Vidal-Moya, S. Wild, A. Doménech-Carbó, B.S.J. Heller, S. Shin, H.P. Steinrück, F. Maier, F. Hauke, M. Varela, A. Hirsch, A. Leyva-Pérez, G. Abellán, Few layer 2D pnictogens catalyze the alkylation of soft nucleophiles with esters, *Nat. Commun.* 10 (2019) 509. <https://doi.org/10.1038/s41467-018-08063-3>.
- [6] N. Antonatos, V. Mazánek, P. Lazar, J. Sturala, Z. Sofer, Acetonitrile-assisted exfoliation of layered grey and black arsenic: contrasting properties, *Nanoscale Adv.* 2 (2020) 1282. <https://doi.org/10.1039/C9NA00754G>.
- [7] X. Liu, L. Xiao, J. Weng, Q. Xu, W. Li, C. Zhao, J. Xu, Y. Zhao, Regulating the reactivity of black phosphorus via protective chemistry, *Sci. Adv.* 6 (2020) 4359. <https://doi.org/10.1126/sciadv.abb4359>.
- [8] L. Niu, J.N. Coleman, H. Zhang, H. Shin, M. Chhowalla, Z. Zheng, Production of two-dimensional nanomaterials via liquid-based direct exfoliation, *Small.* 12 (2016) 272. <https://doi.org/10.1002/sml.201502207>.
- [9] M.B. Erande, S.R. Suryawanshi, M.A. More, D.J. Late, Electrochemically exfoliated black phosphorus nanosheets - prospective field emitters, *Eur. J. Inorg. Chem.* 2015 (2015) 3102. <https://doi.org/10.1002/ejic.201500145>.
- [10] A.M.L. Marzo, R. Gusmão, Z. Sofer, M. Pumera, Towards antimonene and 2d antimony telluride through electrochemical exfoliation, *Chem. – A Eur. J.* 26 (2020) 6583. <https://doi.org/10.1002/chem.201905245>.
- [11] Y. Zhang, X. Zhang, Y. Ling, F. Li, A.M. Bond, J. Zhang, Controllable synthesis of few-layer bismuth subcarbonate by electrochemical exfoliation for enhanced CO<sub>2</sub> reduction performance, *Angew. Chemie - Int. Ed.* 57 (2018) 13283. <https://doi.org/10.1002/anie.201807466>.
- [12] E. Tan, B.L. Li, K. Ariga, C.T. Lim, S. Garaj, D.T. Leong, Toxicity of two-dimensional layered materials and their heterostructures, *Bioconjug. Chem.* 30 (2019) 2287. <https://doi.org/10.1021/acs.bioconjchem.9b00502>.

- [13] H.L. Chia, N.M. Latiff, R. Gusmão, Z. Sofer, M. Pumera, Cytotoxicity of shear exfoliated pnictogen (As, Sb, Bi) nanosheets, *Chem. - A Eur. J.* 25 (2019) 2242. <https://doi.org/10.1002/chem.201804336>.
- [14] S.M. Beladi-Mousavi, J. Plutnar, M. Pumera, Near-atomic-thick bismuthene oxide microsheets for flexible aqueous anodes: Boosted performance upon 3D → 2D transition, *ACS Appl. Mater. Interfaces* 12 (2020) 55936. <https://dx.doi.org/10.1021/acsami.0c16802>.
- [15] P. Ares, F. Aguilar-Galindo, D. Rodríguez-San-Miguel, D.A. Aldave, S. Díaz-Tendero, M. Alcamí, F. Martín, J. Gómez-Herrero, F. Zamora, Mechanical isolation of highly stable antimonene under ambient conditions, *Adv. Mater.* 28 (2016) 6332. <https://dx.doi.org/10.1002/adma.201602128>.
- [16] C. Gibaja, M. Assebban, I. Torres, M. Fickert, R. Sanchis-Gual, I. Brotons, W.S. Paz, J.J. Palacios, E.G. Michel, G. Abellán, F. Zamora, Liquid phase exfoliation of antimonene: systematic optimization, characterization and electrocatalytic properties, *J. Mater. Chem. A* 7 (2019) 22475. <https://doi.org/10.1039/c9ta06072c>.
- [17] Z. Sofer, D. Sedmidubský, Š. Huber, J. Luxa, D. Bouša, C. Boothroyd, M. Pumera, Layered black phosphorus: Strongly anisotropic magnetic, electronic, and electron-transfer properties, *Angew. Chemie Int. Ed.* 55 (2016) 3382. <https://doi.org/10.1002/anie.201511309>.
- [18] P. Marvan, Š. Huber, J. Luxa, V. Mazánek, D. Sedmidubský, Z. Sofer, M. Pumera, Edge vs. basal plane electrochemistry of layered pnictogens (As, Sb, Bi): Does edge always offer faster electron transfer?, *Appl. Mater. Today.* 16 (2019) 179. <https://doi.org/10.1016/j.apmt.2019.05.009>.
- [19] R. Gusmão, Z. Sofer, D. Bouša, M. Pumera, Black phosphorus synthesis path strongly influences its delamination, chemical properties and electrochemical performance, *ACS Appl. Energy Mater.* 1 (2018) 503. <https://doi.org/10.1021/acsaem.7b00106>.
- [20] R. Gusmão, Z. Sofer, D. Bouša, M. Pumera, Pnictogen (As, Sb, Bi) nanosheets for electrochemical applications are produced by shear exfoliation using kitchen blenders, *Angew. Chem. Int. Ed.* 56 (2017) 14417. <https://doi.org/10.1002/anie.201706389>.
- [21] C.C. Mayorga-Martinez, Z. Sofer, D. Sedmidubský, J. Luxa, B. Kherzi, M. Pumera, Metallic impurities in black phosphorus nanoflakes prepared by different synthetic routes, *Nanoscale.* 10 (2018) 1540. <https://doi.org/10.1039/c7nr05718k>.
- [22] Y. Yao, H. Zhang, J. Sun, W. Ma, L. Li, W. Li, J. Du, Novel QCM humidity sensors using stacked black phosphorus nanosheets as sensing film, *Sensor. Actuator. B Chem.* 244 (2017) 259. <http://dx.doi.org/10.1016/j.snb.2017.01.010>.
- [23] D.T. Phan, I.O. Park, A.R. Park, C.M. Park, K.J. Jeon, Black P/graphene hybrid: A fast response humidity sensor with good reversibility and stability, *Sci. Rep.* 7 (2017) 10561 <http://dx.doi.org/10.1038/s41598-017-10848-3>.
- [24] C.M. Chen, J. Xu, Y. Yao, SIW resonator humidity sensor based on layered black phosphorus, *Electron. Lett.* 53 (2017) 249. <http://dx.doi.org/10.1049/el.2016.3844>.

- [25] J. Miao, L. Cai, S. Zhang, J. Nah, J. Yeom, C. Wang, Air-stable humidity sensor using few-layer black phosphorus, *ACS Appl. Mater. Interfaces* 9 (2017) 10019. <http://dx.doi.org/10.1021/acsami.7b01833>.
- [26] S. Walia, Y. Sabri, T. Ahmed, M.R. Field, R. Ramanathan, A. Arash, S.K. Bhargava, S. Sriram, M. Bhaskaran, V. Bansal, S. Balendhran, Defining the role of humidity in the ambient degradation of few-layer black phosphorus, *2D Mater.* 4 (2017) 015025. <http://dx.doi.org/10.1088/2053-1583/4/1/015025>.
- [27] P. He, J.R. Brent, H. Ding, J. Yang, D.J. Lewis, P. O'Brien, B. Derby, Fully printed high performance humidity sensors based on two-dimensional materials, *Nanoscale* 10 (2018) 5599. <http://dx.doi.org/10.1039/c7nr08115d>.
- [28] Z. Liu, J. Huang, Q. Wang, J. Zhou, J. Ye, X. Li, Y. Geng, Z. Liang, Y. Du, X. Tian, Indium oxide-black phosphorus composites for ultrasensitive nitrogen dioxide sensing at room temperature, *Sensor. Actuator. B Chem.* 308 (2020) 127650. <https://doi.org/10.1016/j.snb.2019.127650>.
- [29] G. Lee, S. Kim, S. Jung, S. Jang, J. Kim, Suspended black phosphorus nanosheet gas sensors, *Sensor. Actuator. B Chem.* 250 (2017) 569. <http://dx.doi.org/10.1016/j.snb.2017.04.176>.
- [30] Y. Wang, J. Xue, X. Zhang, J. Si, Y. Liu, L. Ma, M. Ullah, M. Ikram, L. Li, K. Shi, Novel intercalated CuO/black phosphorus nanocomposites: Fabrication, characterization and NO<sub>2</sub> gas sensing at room temperature. *Mater. Sci. Semicond. Process* 110 (2020) 104961. <https://doi.org/10.1016/j.mssp.2020.104961>.
- [31] W. Yuan, Y. Tang, K. Yang, Z. Hua, F. Yin, D. Xia, Gas sensing investigation on anthraquinone nanowire decorated phosphorene: Enhanced stability in conjunction with superior sensitivity, *Chem. Eng. J.* 394 (2020) 124933. <https://doi.org/10.1016/j.cej.2020.124933>.
- [32] Y. Tang, K. Yang, Z. Hua, F. Yin, W. Yuan, A new sensing material design based on chemically passivated phosphorene/porous two-dimensional polymer: Highly sensitive and selective detection of NO<sub>2</sub>, *Sensor. Actuator. B Chem.* 329 (2021) 129233. <https://doi.org/10.1016/j.snb.2020.129233>.
- [33] S.Y. Cho, H.J. Koh, H.W. Yoo, H.T. Jung, Tunable chemical sensing performance of black phosphorus by controlled functionalization with noble metals, *Chem. Mater.* 29 (2017) 7197. <https://doi.org/10.1021/acs.chemmater.7b01353>.
- [34] G. Lee, S. Jung, S. Jang, J. Kim, Platinum-functionalized black phosphorus hydrogen sensors, *Appl. Phys. Lett.* 110 (2017) 242103. <https://doi.org/10.1063/1.4985708>.
- [35] P. Li, D. Zhang, C. Jiang, X. Zong, Y. Cao, Ultra-sensitive suspended atomically thin-layered black phosphorus mercury sensors, *Biosens. Bioelectron.* 98 (2017) 68. <http://dx.doi.org/10.1016/j.bios.2017.06.027>.
- [36] G. Zhou, H. Pu, J. Chang, X. Sui, S. Mao, J. Chen, Real-time electronic sensor based on black phosphorus/Au NPs/DTT hybrid structure: Application in arsenic detection, *Sensor. Actuator. B Chem.* 257 (2018) 214. <https://doi.org/10.1016/j.snb.2017.10.132>.

- [37] P. Li, D. Zhang, J. Wu, Y. Cao, Z. Wu, Flexible integrated black phosphorus sensor arrays for high performance ion sensing, *Sensor. Actuator. B Chem.* 273 (2018) 358. <https://doi.org/10.1016/j.snb.2018.06.077>.
- [38] J. Chang, A. Maity, H. Pu, X. Sui, G. Zhou, R. Ren, G. Lu, J. Chen, Impedimetric phosphorene field-effect transistors for rapid detection of lead ions, *Nanotechnology* 29 (2018) 375501. <https://doi.org/10.1088/1361-6528/aac66a>.
- [39] H.D. Wang, D.K. Sang, Z.N. Guo, R. Cao, J.L. Zhao, M.N.U. Shah, T.J. Fan, D.Y. Fan, H. Zhang, Black phosphorus-based field effect transistor devices for Ag ions detection. *Chin. Phys. B* 27 (2018) 087308. <https://doi.org/10.1088/1674-1056/27/8/087308>.
- [40] Z. Zhuge, Y. Tang, J. Tao, Y. Zhao, Functionalized black phosphorus nanocomposite for biosensing, *ChemElectroChem* 6 (2019) 1129. <https://doi.org/10.1002/celec.201801439>.
- [41] X. Li, X. Niu, W. Zhao, W. Chen, C. Yin, Y. Men, G. Li, W. Sun, Black phosphorene and PEDOT:PSS-modified electrode for electrochemistry of hemoglobin, *Electrochem. Commun.* 86 (2018) 68. <https://doi.org/10.1016/j.elecom.2017.11.017>.
- [42] Y. Zhao, Y.H. Zhang, Z. Zhuge, Y.H. Tang, J.W. Tao, Y. Chen, Synthesis of a poly-L-lysine/black phosphorus hybrid for biosensors, *Anal. Chem.* 90 (2018) 3149. <https://doi.org/10.1021/acs.analchem.7b04395>.
- [43] H. Ding, L. Zhang, Z. Tang, Y. Dong, X. Chu, Black phosphorus quantum dots doped ZnO nanoparticles as efficient electrode materials for sensitive hydrogen peroxide detection, *J. Electroanal. Chem.* 824 (2018) 161. <https://doi.org/10.1016/j.jelechem.2018.07.055>.
- [44] X. Li, G. Luo, H. Xie, Y. Niu, X. Li, R. Zou, Y. Xi, Y. Xiong, W. Sun, G. Li, Voltammetric sensing performances of a carbon ionic liquid electrode modified with black phosphorene and hemin, *Microchim. Acta* 186 (2019) 304. <https://doi.org/10.1007/s00604-019-3421-x>.
- [45] P.K. Sarswat, Y.K. Mishra, M.L. Free, Fabrication and response of alpha-hydroxybutyrate sensors for rapid assessment of cardiometabolic disease risk, *Biosens. Bioelectron.* 89 (2017) 334. <http://dx.doi.org/10.1016/j.bios.2016.07.019>.
- [46] J. Cai, B. Sun, W. Li, X. Gou, Y. Gou, D. Li, F. Hu, Novel nanomaterial of porous graphene functionalized black phosphorus as electrochemical sensor platform for bisphenol A detection, *J. Electroanal. Chem.* 835 (2019) 1. <https://doi.org/10.1016/j.jelechem.2019.01.003>.
- [47] L. Wu, Q. Meng, Z. Xu, Q. Cao, Y. Xiao, H. Liu, G. Han, S. Wei, Passivation of black phosphorus as organic-phase enzyme platform for bisphenol A determination, *Anal. Chim. Acta* 1095 (2020) 197. <https://doi.org/10.1016/j.aca.2019.10.030>.
- [48] Y. Xiang, M.B. Camarada, Y. Wen, H. Wu, J. Chen, M. Li, X. Liao, Simple voltammetric analyses of ochratoxin A in food samples using highly-stable and anti-fouling black phosphorene nanosensor, *Electrochim. Acta* 282 (2018) 490. <https://doi.org/10.1016/j.electacta.2018.06.055>.

- [49] Y. Ge, M.B. Camarada, L. Xu, M. Qu, H. Liang, E. Zhao, M. Li, Y. Wen, A highly stable black phosphorene nanocomposite for voltammetric detection of clenbuterol, *Microchim. Acta* 185 (2018) 566. <https://doi.org/10.1007/s00604-018-3084-z>.
- [50] Y. Ge, M. Qu, L. Xu, X. Wang, J. Xin, X. Liao, M. Li, M. Li, Y. Wen, Phosphorene nanocomposite with high environmental stability and antifouling capability for simultaneous sensing of clenbuterol and ractopamine, *Microchim. Acta* 186 (2019) 836. <https://doi.org/10.1007/s00604-019-3908-5>.
- [51] S. Ramalingam, R. Chand, C.B. Singh, A. Singh, Phosphorene-gold nanocomposite based microfluidic aptasensor for the detection of okadaic acid, *Biosens. Bioelectron.* 135 (2019) 14. <https://doi.org/10.1016/j.bios.2019.03.056>.
- [52] X. Niu, W. Weng, C. Yin, Y. Niu, G. Li, R. Dong, Y. Men, W. Sun, Black phosphorene modified glassy carbon electrode for the sensitive voltammetric detection of rutin, *J. Electroanal. Chem.* 811 (2018) 78. <https://doi.org/10.1016/j.jelechem.2018.01.038>.
- [53] Y. Chen, R. Ren, H. Pu, J. Chang, S. Mao, J. Chen, Field-effect transistor biosensors with two-dimensional black phosphorus nanosheets, *Biosens. Bioelectron.* 89 (2017) 505. <http://dx.doi.org/10.1016/j.bios.2016.03.059>.
- [54] J. Cai, X. Gou, B. Sun, W. Li, D. Li, J. Liu, F. Hu, Y. Li, Porous graphene-black phosphorus nanocomposite modified electrode for detection of leptin, *Biosens. Bioelectron.* 137 (2019) 88. <https://doi.org/10.1016/j.bios.2019.04.045>.
- [55] S. Liang, L. Wu, H. Liu, J. Li, M. Chen, M. Zhang, Organic molecular passivation of phosphorene: An aptamer-based biosensing platform, *Biosens. Bioelectron.* 126 (2019) 30. <https://doi.org/10.1016/j.bios.2018.10.037>.
- [56] Y. Sun, H. Jin, X. Jiang, R. Gui, Black phosphorus nanosheets adhering to thionine-doped 2D MOF as a smart aptasensor enabling accurate capture and ratiometric electrochemical detection of target microRNA, *Sensor. Actuator. B Chem.* 309 (2020) 127777. <https://doi.org/10.1016/j.snb.2020.127777>.
- [57] J. Zou, J.G. Yu, Nafion-stabilized black phosphorus nanosheets-maltosyl- $\beta$ -cyclodextrin as a chiral sensor for tryptophan enantiomers, *Mater. Sci. Eng. C* 112 (2020) 110910. <https://doi.org/10.1016/j.msec.2020.110910>.
- [58] T. Xue, Y. Sheng, J. Xu, Y. Li, X. Lu, Y. Zhu, X. Duan, Y. Wen, In-situ reduction of  $\text{Ag}^+$  on black phosphorene and its  $\text{NH}_2$ -MWCNT nanohybrid with high stability and dispersibility as nanozyme sensor for three ATP metabolites, *Biosens. Bioelectron.* 145 (2019) 111716. <https://doi.org/10.1016/j.bios.2019.111716>.
- [59] Z. Zhang, Y. Li, J. Xu, Y. Wen, Electropolymerized molecularly imprinted polypyrrole decorated with black phosphorene quantum dots onto poly (3, 4-ethylenedioxythiophene) nanorods and its voltammetric sensing of vitamin C, *J. Electroanal. Chem.* 814 (2018) 153. <https://doi.org/10.1016/j.jelechem.2018.02.059>.
- [60] K.J. Tian, L. Hu, Y.P. Dong, X.F. Chu, Application of black phosphorus nanosheets modified electrode for electrochemical determination of ascorbic acid, *Russ. J. Electrochem.* 55 (2019) 1221. <https://doi.org/10.1134/S1023193519120176>.

- [61] L. Wu, Z. Xu, Q. Meng, Y. Xiao, Q. Cao, B. Rathi, H. Liu, G. Han, J. Zhang, J. Yan, A new aptamer/black phosphorous interdigital electrode for malachite green detection, *Anal. Chim. Acta* 1099 (2020) 39. <https://doi.org/10.1016/j.aca.2019.11.026>.
- [62] H. Liang, H. Xu, Y. Zhao, J. Zheng, H. Zhao, G. Li, C.P. Li, Ultrasensitive electrochemical sensor for prostate specific antigen detection with a phosphorene platform and magnetic covalent organic framework signal amplifier, *Biosens. Bioelectron.* 144 (2019) 111691. <https://doi.org/10.1016/j.bios.2019.111691>.
- [63] H. Xu, J. Zheng, H. Liang, C.P. Li, Electrochemical sensor for cancer cell detection using calix[8]arene/polydopamine/phosphorene nanocomposite based on host-guest recognition, *Sensor. Actuator. B Chem.* 317 (2020) 128193. <https://doi.org/10.1016/j.snb.2020.128193>.
- [64] D. Fang, D. Zhao, S. Zhang, Y. Huang, H. Dai, Y. Lin, Black phosphorus quantum dots functionalized MXenes as the enhanced dual-mode probe for exosomes sensing. *Sensor. Actuator. B Chem.* 305 (2020) 127544. <https://doi.org/10.1016/j.snb.2019.127544>.
- [65] H. Liu, Y. Zhang, Y. Dong, X. Chu, Electrogenated chemiluminescence aptasensor for lysozyme based on copolymer nanospheres encapsulated black phosphorus quantum dots, *Talanta* 199 (2019) 507. <https://doi.org/10.1016/j.talanta.2019.02.099>.
- [66] Y. Wang, H. Shi, L. Zhang, S. Ge, M. Xu, X. Wang, J. Yu, Two-dimensional black phosphorus nanoflakes: A coreactant-free electrochemiluminescence luminophors for selective Pb<sup>2+</sup> detection based on resonance energy transfer, *J. Hazard. Mater.* 403 (2020) 123601. <https://doi.org/10.1016/j.jhazmat.2020.123601>.
- [67] T. Ahmed, S. Balendhran, M.N. Karim, E.L.H. Mayes, M.R. Field, R. Ramanathan, M. Singh, V. Bansal, S. Sriram, M. Bhaskaran, S. Walia, Degradation of black phosphorus is contingent on UV – blue light exposure, *npj 2D Mater. Appl.* 1 (2017) 18. <https://doi.org/10.1038/s41699-017-0023-5>.
- [68] C. C. Mayorga-Martinez, R. Gusmão, S. Zdenek, M. Pumera, Pnictogen-based enzymatic phenol biosensors : phosphorene, arsenene, antimonene, and bismuthene, *Angew. Chem. Int. Ed.* 58 (2019) 134. <https://doi.org/10.1002/anie.201808846>.
- [69] T. Garcia-Mendiola, C. Gutiérrez-Sánchez, C. Gibaja, I. Torres, C. Busó-Rogero, F. Pariente, J. Solera, Z. Razavifar, J.J. Palacios, F. Zamora, E. Lorenzo, Functionalization of few-layer antimonene with oligonucleotides for DNA sensing, *ACS Appl. Nano Mater.* 3 (2020) 3625. <https://dx.doi.org/10.1021/acsnm.0c00335>.
- [70] B. Fatima, D. Hussain, S. Bashir, H.T. Hussain, R. Aslam, R. Nawaz, H.N. Rashid, N. Bashir, S. Majeed, M.N. Ashiq, M. Najam-ul-Haq, Catalase immobilized antimonene quantum dots used as an electrochemical biosensor for quantitative determination of H<sub>2</sub>O<sub>2</sub> from CA-125 diagnosed ovarian cancer samples, *Mater. Sci. Eng. C* 117 (2020) 111296. <https://doi.org/10.1016/j.msec.2020.111296>.
- [71] H.L. Chia, C.C. Mayorga-Martínez, R. Gusmao, F. Novotny, R.D. Webster, M. Pumera, A highly sensitive enzyme-less glucose sensor based on pnictogens and silver shell-gold core nanorod composites, *Chem. Commun.* 56 (2020) 7909. <https://doi.org/10.1039/d0cc02770g>.

- [72] S.M. Beladi-Mousavi, A.M. Pourrahimi, Z. Sofer, M. Pumera, Atomically thin 2D-arsenene by liquid-phased exfoliation: toward selective vapor sensing, *Adv. Funct. Mater.* 29 (2019) 1807004. <https://doi.org/10.1002/adfm.201807004>.
- [73] A.C. Lazanas, K. Tsirka, A.S. Paipetis, M.I. Prodromidis, 2D bismuthene/graphene modified electrodes for the ultra-sensitive stripping voltammetric determination of lead and cadmium, *Electrochim. Acta* 336 (2020) 135726. <https://doi.org/10.1016/j.electacta.2020.135726>.
- [74] M.A. Tapia, C. Pérez-Ràfols, R. Gusmão, N. Serrano, Z. Sofer, J.M. Díaz-Cruz, Enhanced voltammetric determination of metal ions by using a bismuthene-modified screen-printed electrode, *Electrochim. Acta* 362 (2020) 137144. <https://doi.org/10.1016/j.electacta.2020.137144>.
- [75] K. S. Novoselov, A. Mishchenko, A. Carvalho, A.H. Castro Neto, 2D materials and van der Waals heterostructures, *Science* 353 (2016) aac9439. <https://doi.org/10.1126/science.aac9439>.
- [76] M. Chhowalla, D. Jena, H. Zhang, Two-dimensional semiconductors for transistors, *Nat. Rev. Mater.* 1 (2016) 16052. <https://doi.org/10.1038/natrevmats.2016.52>.
- [77] P. K. Roy, J. Luxa, Z. Sofer, Emerging pnictogen-based 2D semiconductors: sensing and electronic devices, *Nanoscale* 12 (2020) 10430. <https://doi.org/10.1039/d0nr02932g>.

**Table 1.** Phosphorene -based sensors for gas sensing electrochemical applications.

Ref.	Sensor Type	Analyte	Sensor characteristics	Tested range	Additional information
[22]	BP nanosheets-QCM	Humidity	<ul style="list-style-type: none"> <li>• Change in resonance frequency: 863 Hz (QCM-2 <math>\mu\text{L}</math> BP), 1698 Hz (QCM-4 <math>\mu\text{L}</math> BP), and 3145 Hz (QCM-6 <math>\mu\text{L}</math> BP) in the RH of 11.3-97.3%.</li> <li>• Stability (<math>R_{\text{crystal}}</math> value): within 30 <math>\Omega</math> in the RH of 11.3-84.3%.</li> <li>• Humidity hysteresis: less than 4% RH over the entire RH of 11.3-97.3%.</li> <li>• Response times: 14 s (QCM-2 <math>\mu\text{L}</math> BP), 23 s (QCM-4 <math>\mu\text{L}</math> BP), and 29 s (QCM-6 <math>\mu\text{L}</math> BP).</li> <li>• Recovery times<sup>a</sup>: within 10 s.</li> </ul>	RH of 11.3-97.3% or 11.3-84.3% depending on the studied characteristic	<ul style="list-style-type: none"> <li>• The humidity sensing characteristics are studied by using an oscillating circuit method.</li> <li>• QCM-6 <math>\mu\text{L}</math> BP sensor shows the largest resonance frequency response for a given change in humidity due to the greater amount of BP used.</li> <li>• The stability of the BP based QCM sensor with a large amount of BP nanosheets becomes worse at extra high humidity environment.</li> <li>• The QCM-4 <math>\mu\text{L}</math> BP is more suitable for high humidity level detection.</li> </ul>
[23]	BP powder– graphene heterojunction sensor	Humidity	<ul style="list-style-type: none"> <li>• Response/recovery time<sup>a</sup>: 9/30 s to BP-graphene sensor and 24/72 s to BP pure sensor at 70% RH.</li> <li>• Sensor relative response (S)<sup>b</sup>: 43.4, 35, 25.1, 13, and 3% with a RH of 70, 55, 40, 25, and 15%, respectively.</li> <li>• Stability: confirmed the linearity in the RH range of 15-70% after 2 weeks.</li> <li>• Good repeatability and non-degradation after 1 h as compared to</li> </ul>	15 - 70% RH	<ul style="list-style-type: none"> <li>• Graphene was transferred onto <math>\text{SiO}_2/\text{Si}</math> with wafer-level. The patterned graphene was located between two Au electrodes.</li> <li>• BP was synthesized by the high energy ball milling technique at ambient temperature and pressure, and deposited on the patterned graphene by electro-spray.</li> <li>• The increasing hole density in p-type BP</li> </ul>

			BP pure sensor.			and graphene encourages the free electron transfer via the BP/graphene interface due to decrease of resistance.
			<ul style="list-style-type: none"> <li>• The BP/graphene sensor response/recovery time is slower after 2 weeks and had a large reduction in response after 4 weeks.</li> <li>• Initial resistance: 7.5 and 500 k<math>\Omega</math> for the BP/graphene and BP pure sample, respectively.</li> </ul>			
[24]	BP layered-SIW resonator sensor	Humidity	<ul style="list-style-type: none"> <li>• Humidity sensitivity: 197.67 kHz/%RH</li> <li>• Maximum <math>S_{11}</math> magnitudes: at RH=11% shows little difference between BP sensor and bare sensor; at RH=97.3% are about -18 dB for BP sensor and -22 dB for bare sensor.</li> </ul>	~11.3 – 97.3% RH		<ul style="list-style-type: none"> <li>• The microwave SIW resonator humidity sensor was drop-coated by 10 <math>\mu</math>L of BP solution on the sensing slots.</li> <li>• The humidity sensitivity of the BP-SIW resonator es about 40 times larger than the sensor without material.</li> <li>• The <math>S_{11}</math> as a peak magnitude decrease with increasing RH, indicating that the dielectric losses increase in both BP and bare sensors, but in BP sensor the increase is smaller than in the bare sensor.</li> </ul>
[25]	BP flakes-FET with Al <sub>2</sub> O <sub>3</sub> passivation.	Humidity	<ul style="list-style-type: none"> <li>• n-branch current variation: <math>\sim 2.3</math> and <math>\sim 260.6</math> nA/<math>\mu</math>m before and after ALD Al<sub>2</sub>O<sub>3</sub>, respectively.</li> <li>• Transconductance variation: <math>\sim 10^{-5}</math> and <math>\sim 10^{-2}</math> <math>\mu</math>S/<math>\mu</math>m before and after ALD Al<sub>2</sub>O<sub>3</sub>, respectively.</li> </ul>	21 - 83% RH		<ul style="list-style-type: none"> <li>• BP-Flakes were passivated by a 6 nm thick Al<sub>2</sub>O<sub>3</sub> encapsulation layer using ALD.</li> <li>• The Al<sub>2</sub>O<sub>3</sub> encapsulation can successfully suppress BP degradation, which leads to drastically improved long-term stability in air with a trade-</li> </ul>

[26]	BP layered-QCM	Humidity	<ul style="list-style-type: none"> <li>• Device hole mobilities: <math>\sim 100 \text{ cm}^2\text{V}^{-1}\text{s}^{-1}</math> after ALD <math>\text{Al}_2\text{O}_3</math>.</li> <li>• Current on-off ratio: <math>\sim 3.4 \times 10^3</math> and <math>\sim 10^4</math> before and after ALD <math>\text{Al}_2\text{O}_3</math>, respectively, at a <math>V_{\text{DS}}=0.5\text{V}</math> (RH <math>\sim 21\%</math> and room temperature).</li> <li>• Dynamic sensing response (<math>V_{\text{DS}}=1 \text{ V}</math>, <math>V_{\text{GS}}=-60 \text{ V}</math>): <math>\sim 3</math>-fold enhancement in <math>I_{\text{DS}}</math> at RH = 82% (without <math>\text{Al}_2\text{O}_3</math> dielectric); <math>\sim 1.7</math>-fold enhancement in <math>I_{\text{DS}}</math> at RH = 81% (with <math>\text{Al}_2\text{O}_3</math> dielectric).</li> </ul>	<p>12.5 - 90% (at 30°C)</p> <p>Dynamic range: 10 – 90% RH</p>	<p>off in slightly reduced sensitivity.</p> <ul style="list-style-type: none"> <li>• The slightly reduced response/sensitivity is caused by the existence of the 6 nm-thick <math>\text{Al}_2\text{O}_3</math> dielectric layer, which weakens the electrical field induced by the electrostatic dipole moment of water molecules.</li> <li>• This study is focused on the individual effects of environmental factors (temperature, light, and humidity), on the deterioration of BP.</li> <li>• Humidity adsorption on BP does not cause degradation, only facilitates photo-oxidation that is the main degradation phenomenon originated at the edges of the BP crystals.</li> <li>• The recoverable humidity sensing capabilities of BP were demonstrated with detection levels down to 10% RH</li> <li>• Just isolating BP from light, its degradation can be significantly retarded and its lifetime protracted in ambient environment</li> </ul>
------	----------------	----------	--	---	---

[27]	BP nanoflakes/Ag interdigitated electrode	Humidity	<ul style="list-style-type: none"> <li>• Sensitivity (S)<sup>d</sup>: <math>5.08 \times 10^3</math>, <math>3.92 \times 10^3</math> and <math>6.29 \times 10^2</math> at 10 Hz, 100 Hz and 1 kHz respectively for RH from 11 to 97%.</li> <li>• Response/recovery time: 4.7/3.0 s respectively <sup>a</sup>.</li> <li>• No noticeable change was observed when the samples were measured in a fixed RH= 11% for about 24 h.</li> </ul>	11 - 97% RH	<ul style="list-style-type: none"> <li>• The sensor device was fabricated by inkjet printing of BP nanoflakes (<math>\sim 0.67 \text{ mg ml}^{-1}</math>) colloidal ink onto the Ag interdigitated electrode.</li> <li>• BP device can be used for sensing small changes (as little as 3 %) in RH .</li> <li>• The capacitance of the BP sensor shows more than one order of magnitude change as a function of fingertip proximity under ambient air conditions, revealing potential applications in contactless switching.</li> <li>• This work also reports de development of a graphene oxide sensor, which is fabricated by printing graphene oxide onto the Ag interdigitated electrode. This sensor also shows a high performance as humidity sensor.</li> </ul>
[28]	BP-In <sub>2</sub> O <sub>3</sub> based sensors	NO <sub>2</sub>	<ul style="list-style-type: none"> <li>• Specific surface area (<math>\text{m}^2 \text{ g}^{-1}</math>): 42.1, 42.7, 44.6, 50.5 for In<sub>2</sub>O<sub>3</sub>, BP-InO-1, BP-InO-2, and BP-InO-3, respectively.</li> <li>• Electron transfer rate (<math>\text{cm}^2 \text{ V}^{-1} \text{ s}^{-1}</math>): 63, 126, 155 and 181 for In<sub>2</sub>O<sub>3</sub>, BP-InO-1, BP-InO-2, and BP-InO-3, respectively.</li> <li>• Maximum sensor response (<math>R_g/R_a</math>)<sup>e</sup>: 604, 233 and 748 for In<sub>2</sub>O<sub>3</sub>, BP-InO-1, BP-InO-2 (5 ppm NO<sub>2</sub> at the optimum operating temperature of 80 °C, 25 °C</li> </ul>	10 ppb – 50 ppm	<ul style="list-style-type: none"> <li>• BP-In<sub>2</sub>O<sub>3</sub> composites were prepared by ultrasonic treatment of BP nanosheets dispersion in the presence of In<sub>2</sub>O<sub>3</sub> nanorods synthesized by the microwave-assisted hydrothermal method.</li> <li>• BP-In<sub>2</sub>O<sub>3</sub> composites were coated onto an Al<sub>2</sub>O<sub>3</sub> tube, on which two Au electrodes was formerly printed.</li> <li>• BP-InO-1, BP-InO-2, and BP-InO-3 have</li> </ul>

			and 25 °C for In <sub>2</sub> O <sub>3</sub> , BP-InO-1 and BP-InO-2)			a BP amount of 0.51 wt%, 1.06 wt% and 1.51 wt%, respectively.
			<ul style="list-style-type: none"> <li>• Response/recovery time<sup>a</sup>: 322/524 s for In<sub>2</sub>O<sub>3</sub> sensor and 170/271 s for BP-InO-2 sensor, respectively.</li> <li>• BP-InO-2 sensor shows a good repeatability and a long-term stability (35 days) for 5 ppm at 25 °C.</li> </ul>			<ul style="list-style-type: none"> <li>• BP-InO-2 sensor exhibits higher response, better selectivity, faster response-recovery behavior, and ultralow detection limit of 10 ppb towards NO<sub>2</sub> at 25 °C compared to In<sub>2</sub>O<sub>3</sub>, other BP-In<sub>2</sub>O<sub>3</sub> compositions and previously reported BP based sensor.</li> </ul>
[29]	Suspended BP flakes sensor  Supported BP flakes sensor	NO <sub>2</sub>	<ul style="list-style-type: none"> <li>• Sensor response (S)<sup>f</sup>: a small difference between the suspended and supported BP sensors is obtained at lower gas concentrations. This difference increases with the gas concentrations (at 200 ppm the gas response was increased by 23%).</li> <li>• Equilibrium constant (Langmuir isotherm): 60.3 and 37.6 for suspended and supported BP sensor, respectively.</li> </ul>	25 – 200 ppm		<ul style="list-style-type: none"> <li>• BP flakes were transferred onto source-drain electrodes through a dry-transfer technique, where the Ti/Au electrodes were pre-patterned on a SiO<sub>2</sub>/Si substrate.</li> <li>• Both sides of BP flakes in the suspended sensors are available for target gases to be adsorbed, unlike conventional supported sensors.</li> <li>• Suspended BP sensor has the advantage of a high surface-to-volume ratio, adsorption areas on both sides and neglected substrate effects, which lead to higher gas response.</li> <li>• Suspended BP sensor shows excellent reproducibility and superior responses to NO<sub>2</sub> (~65%) with a faster desorption rate (two times faster) than the supported BP sensor.</li> </ul>

[30]	CuO/Py-BP NCP/ interdigitated Au electrode	NO <sub>2</sub>	<ul style="list-style-type: none"> <li>• Sensor response (S)<sup>g</sup>: 20.7 at 100 ppm and 1.0 at 0.01 ppm of NO<sub>2</sub> for the CuO/BP-190 sensor at 25 °C and RH=26%.</li> <li>• Response (R<sub>a</sub>/R<sub>g</sub>): 10.4 for the CuO/BP-190 sensor at 100 ppm.</li> <li>• Response/recovery time: 4/42 s at 100 ppm and 1.1/34 s at 0.01 ppm, respectively, for the CuO/BP-190 sensor.</li> <li>• Good repeatability of CuO/BP-190 sensor for 8 cycles at 100 ppm NO<sub>2</sub>.</li> <li>• Long-term stability of the CuO/BP-190 sensor (~11 weeks, tests every 2 weeks at 30 ppm NO<sub>2</sub> at 25 °C).</li> <li>• Limit of detection: 0.01 ppm for CuO/BP-190 and CuO/BP-190-2; and 0.5 ppm for CuO/BP-170 and CuO/BP-210 at RH of 26%.</li> <li>• Good selectivity toward NO<sub>2</sub> with a higher response to NO<sub>2</sub> than to NH<sub>3</sub>, CH<sub>4</sub>, CO and H<sub>2</sub>.</li> </ul>	0.01 – 100 ppm under 26% RH	<ul style="list-style-type: none"> <li>• The NCPs were developed by EBP functionalized by Py for the growth of CuO NPs into the interlayers of EBP.</li> <li>• Different CuO/BP NCPs were synthesized at 170, 190 and 210 °C for 5 h: CuO/BP-170; CuO/BP-190; CuO/BP-190-2 (for 2h); and CuO/BP-210.</li> <li>• CuO/BP NCPs were drop-casted onto an interdigitated Au electrode.</li> <li>• The CuO/BP-190 sensor response is higher than those of the other sensors over the entire NO<sub>2</sub> concentration range.</li> <li>• The improved sensing property can be attributed to the excellent electrical conductivity of the thin layer BP NSs and the structure of the CuO/BP multi heterojunction.</li> </ul>
[31]	AQNW-BP/IE Bare BP/IE	NO <sub>2</sub>	<ul style="list-style-type: none"> <li>• Sensitivity <sup>h</sup>: 570 and 525% for AQNW-P and bare-P sensor, respectively, at 1 ppm NO<sub>2</sub>.</li> <li>• Response/recovery time <sup>i</sup>: 220/300 s at 100 ppb and 35/118 s at 10 ppm NO<sub>2</sub>,</li> </ul>	0.05 – 10 ppm	<ul style="list-style-type: none"> <li>• AQNW-BP was prepared through anti-solvent crystallization of AQ during the BP liquid exfoliation.</li> <li>• AQNW decoration can successfully suppress BP degradation leading to a</li> </ul>

respectively.

- Recovery > 95% with NO<sub>2</sub> concentration higher than 0.7 ppm.
- AQNW-BP/IE and bare BP/IE show a minimal degradation during long-time NO<sub>2</sub> exposure.
- The sensitivity of AQNW-BP/IE progressively enhanced as increasing the aging time. The sensitivity of AQNW-BP doubled that of the fresh one after 12 days of the sensing film fabrication. Then, a regular sensitivity decrease was detected upon further aging.
- The sensitivity of BP/IE increased by 25% during the first day, and after that the sensitivity progressively decreased and faded in 1 week.
- Good selectivity towards NO<sub>2</sub>, although a slight response was detected upon exposure to NH<sub>3</sub>.

sensing film with enhanced air stability and suitable sensitivity.

- The sensitivity enhancement observed for both sensors during initial aging is due to the increase of oxygen defects.
- AQNW-BP/IE showed better selectivity, sensitivity and sensing speed than Bare BP/IE and other sensors based on graphene and MXene.

[32] Pristine-BP/IE  
CPP/IE  
CPP/T-2DP/IE

NO<sub>2</sub>, NH<sub>3</sub>

- Sensor response (R)<sub>i</sub>: 400, 700 and 2410% for pristine-BP/IE, CPP/IE and CPP/T-2DP/IE respectively, at 1 ppm NO<sub>2</sub>.
- Sensor response (R)<sub>i</sub>: 1326 and 5500% for CPP/IE and CPP/T-2DP/IE respectively, at 1 ppm NO<sub>2</sub>, after 10

0.03 – 5 ppm  
(NO<sub>2</sub>)

- CPP is based on 4-methoxybenzenediazonium modified BP.
- CPP/T-2DP simultaneously overcomes the BP oxidation propensity and improves the gas sensing property.
- In comparison to pristine-BP/IE, CPP/T-

days of ambient exposure.

- Good stability: sensor response ( $R^j$ ) had < than 8% fluctuation as RH increased from 0-60%. From 60 – 96 % the response decreased to 715% for CPP/T-2DP/IE at 1 ppm  $\text{NO}_2$  in air.
- Response/recovery time: 80/246 s, 84/192 s and 67/95 s for pristine–BP, CPP/IE and CPP/T-2DP/IE respectively at 1 ppm  $\text{NO}_2$ .
- Response/recovery time: 240/300 s, and 36/150 s with  $\text{NO}_2$  concentration increasing from 0.03 to 5 ppm, respectively, for the CPP/T-2DP/IE.
- Percent recovery<sup>k</sup>: ~100% at  $\text{NO}_2$  concentration > than 1 ppm at RH~60%.
- Equilibrium constant (Langmuir isotherm): 2.85 for CPP/T-2DP sensor.
- $\text{NO}_2/\text{NH}_3$  response ratio: 6.2, 15.5, 35.6 for pristine–BP, CPP/IE and CPP/T-2DP/IE, respectively.
- $\text{NO}_2$ /water vapor (100% RH) response ratio: 11.9 for CPP/T-2DP/IE.
- Long-term stability: sensing capability for 5 days for pristine-P sensor and >20 days for CPP/IE and CPP/T-2DP/IE.

2DP/IE presents a 6-folds increase in  $\text{NO}_2$  sensitivity caused by the presence of porous T-2DP nanopacers.

- T-2DP nanosheets prevent the dense stacking of BP layers whilst providing abundant gas pathway for adsorption and desorption.
- These 3 sensors were also sensitive to  $\text{NH}_3$  with a negative response (see  $\text{NO}_2/\text{NH}_3$  response ratio).
- The sensor response reveals a time dependent increase during the first several days that can be attributed to the formation of slight oxidation state, which enables the gas adsorption or charge transfer within the sensing film.
- CPP/T-2DP/IE showed increased ambient stability, improved sensing speed, good selectivity, excellent flexibility for  $\text{NO}_2$  detection and detection limit of 0.03 ppm.

<p>[33] Pristine BP flakes sensor Au NPs/BP flakes sensor Pt NPs/BP flakes sensor</p>	<p>NO<sub>2</sub>, H<sub>2</sub>, Ethanol, Toluene, Hexane, Acetone, Acetaldehyde</p>	<ul style="list-style-type: none"> <li>• Au/BP sensor resistance variation<sup>l</sup>: -5% and 0.1% for 5:1 and 2:1 (BP:Au), respectively, at 1 ppm NO<sub>2</sub>.</li> <li>• Pt/BP sensor resistance variation<sup>l</sup>: 5% and 500% for 2:1 (BP:Pt) at 10 ppm and 1% of H<sub>2</sub>, respectively.</li> <li>• Pristine BP sensor resistance variation<sup>l</sup>: 6% at 1000 ppm of ethanol and -70% at 1 ppm of NO<sub>2</sub>.</li> <li>• Baseline resistance: ~0.5% for pristine BP sensor and ~0.01% for Au/BP sensor.</li> <li>• Long-term stability (30 days, intermittent tests, ~ 23°C and ~35 %RH): stable gas response amplitude<sup>m</sup> for Pt/BP sensor to H<sub>2</sub> with a level of ~500% and for Au/BP sensor to NO<sub>2</sub> with a level of 1%. Pristine BP sensor undergoes surface degradation after a month.</li> </ul>	<p>1 - 50 ppm (NO<sub>2</sub>) with Au/BP sensor. 10 - 10000 ppm (H<sub>2</sub>) with Pt/BP sensor.</p>	<ul style="list-style-type: none"> <li>• The chemical sensing implications of Au and Pt incorporation into BP were reported.</li> <li>• Thin films of pristine BP, Au/BP or Pt/BP were attached onto a μ-electrode-printed substrate.</li> <li>• Incorporation concentration from a 5:1 to a 2:1 ratio of BP to Ag or Pt was considered.</li> <li>• Gas sensing ability of BP was improved by functionalization BP with Ag and Pt.</li> <li>• Pt/BP sensor showed a highly sensitive and selective response to 1% H<sub>2</sub> with a channel resistance variation<sup>l</sup> of ~500%.</li> <li>• Ag/BP sensor led to a tunable response toward NO<sub>2</sub> varied from negative to positive. Moreover, the baseline noise level is 50 times improve in comparison to that of pristine BP sensor.</li> </ul>
<p>[34] PMMA/Pt NPs coated BP flakes FET sensor</p>	<p>H<sub>2</sub></p>	<ul style="list-style-type: none"> <li>• μ<sub>eff</sub> and I<sub>ON</sub>/I<sub>OFF</sub> ratio increased by 15.6% and 115%, respectively, after being exposed to 4% H<sub>2</sub>.</li> <li>• Resistive sensitivity (S)<sup>f</sup>: ~50% after being exposed to 4% H<sub>2</sub> at room temperature.</li> </ul>	<p>2000 ppm – 4%</p>	<ul style="list-style-type: none"> <li>• The presented sensor was fabricated by functionalizing the surface of BP flakes using Pt NPs. Then, PMMA was also coated to prevent the degradation of BP in an ambient air and increasing the stability of Pt NPs by reducing catalytic surface ignition effects.</li> </ul>

- Reproducible sensitivity (S)<sup>f</sup> of ~15% and ~4% with a fast response and decay characteristics at 6000 ppm and 2000 ppm of H<sub>2</sub>, respectively, in oxygen ambient (dry air).
- Operating temperature range: 20 – 100 °C.
- The fabricated sensors exhibited reproducible response for up to 6 h.
- The gas response obtained with varying H<sub>2</sub> concentrations well-fitted using the Langmuir isotherm model, indicating that the dominant sensing mechanism in the Pt NPs coated BP sensors corresponds to catalytic-assisted hydrogen dissociation.
- The sensitivity and adsorption rate of the sensors increased with an increase in the operating temperature.

ALD: atomic layer deposition; AQNW: anthraquinone nanowire; BP: black phosphorous; CPP: chemically passivated phosphorene; EBP: expanded black phosphorous; FET: field-effect transistor; I<sub>DS</sub>: source-drain current; IE: interdigitated electrodes; NCP: nanocomposite; NPs: nanoparticles; NSs: nanosheets; PMMA: poly(methyl methacrylate); Py: pyrrole; QCM: quartz crystal microbalance; RH: humidity range; R<sub>a</sub>/R<sub>g</sub>: resistance<sub>air</sub>/resistance<sub>target gas</sub>; R<sub>g</sub>/R<sub>a</sub>: resistance<sub>target gas</sub>/resistance<sub>air</sub>; RSD: relative standard deviation; S: sensor relative response; S<sub>11</sub>: reflection coefficient; SIW: substrate integrated waveguide; T-2DP: porous triazine 2D polymer; V<sub>DS</sub>: drain - source voltage; V<sub>GS</sub>: gate – source voltage; %wt: weight (%); μ<sub>eff</sub>: field - effect mobility.

<sup>a</sup> Response and recovery time: time required by sensor to reach the 90% of the total resistance change (ΔR) when the sensor is exposed to a given target gas in the case of adsorption and desorption respectively.

<sup>b</sup> S(%)= ΔR/R<sub>a</sub> x 100 = (R<sub>h</sub> – R<sub>a</sub>)/R<sub>a</sub> x 100 where R<sub>a</sub> is the resistance of the sensors in the presence of dry N<sub>2</sub> gas, and R<sub>h</sub> is the resistance in the presence of target gas at a given concentration.

<sup>c</sup> Δf= f<sub>0</sub> – f =  $\frac{2 f_0^2}{A \sqrt{\mu_q \rho_q}} \Delta m$ , where f<sub>0</sub> is the natural frequency and f is the resonant frequency after adsorption, A is the active surface area of the QCM electrode, μ<sub>q</sub> is the shear modulus (2.947×10<sup>11</sup> g cm<sup>-1</sup> s<sup>-1</sup>) and ρ<sub>q</sub> is the density (2.648 g cm<sup>-3</sup>) of the quartz crystal.

<sup>d</sup> S = (C<sub>x</sub> – C<sub>11</sub>)/C<sub>11</sub>, where C<sub>x</sub> is the capacitance at x% RH and C<sub>11</sub> is the capacitance at 11% RH.

<sup>e</sup> The sensor response is defined as R<sub>g</sub>/R<sub>a</sub> for oxidizing gas, where R<sub>g</sub> and R<sub>a</sub> stand for the electrical resistances of sensor in the target gas and in air.

<sup>f</sup>  $S(\%) = \Delta R/R_0 \times 100 = (R_0 - R_{\text{exposure}})/R_0 \times 100$ , where  $R_0$  is the resistance of the sensor prior to exposure, and  $R_{\text{exposure}}$  is the resistance in the presence of target gas molecules.

<sup>g</sup>  $S(\%) = R_a/R_g \times 100\%$ , where  $R_a$  is the resistance of the sensor in air, and  $R_g$  is the resistance in the test gas.

<sup>h</sup> Sensitivity is the relative conductance variation, which is defined as  $\Delta G/G_0$  (%), where  $G_0$  is the conductance in balanced gas ( $N_2$ ), and  $\Delta G$  is the conductance variation after exposure to the target gas.

<sup>i</sup> The response time is defined as the time interval that is consumed to reach 90% of the maximum response, and the recovery time is defined as the time period required to return 80% of the baseline level.

<sup>j</sup> The sensor response was defined as  $R = (G_{ns} - G_n)/G_n \times 100\%$ , where  $G_n$  and  $G_{ns}$  are the conductance in  $N_2$  (balanced gas) and sample gas, respectively.

<sup>k</sup> *Percent recovery (%) =  $(G_{ns} - G_r)/(G_{ns} - G_n) \times 100\%$* , where  $G_n$ ,  $G_{ns}$  and  $G_r$  represents the conductance in  $N_2$ , in sample gas, and the recovery conductance after purging with balanced gas, respectively

<sup>l</sup> Resistance variation (%) =  $\Delta R/R_b$ , where  $R_b$  and  $\Delta R$  represent the baseline resistances of each sensor and the change in resistance after exposure to gas molecules, respectively.

<sup>m</sup> Gas sensing amplitude (%) =  $(\Delta R/R_b)_{\text{max}}$ , where  $R_b$  and  $\Delta R$  represent the baseline resistances of each sensor and the change in resistance after exposure to gas molecules, respectively.

**Table 2.** Phosphorene -based sensors for non-gas sensing electrochemical applications.

Ref.	Sensor Type	Analyte	Sample	Technique	Detection limit	Linear range	Additional information
[35]	BP FET on SiO <sub>2</sub> Suspended BP FET	Hg(II)	Spiked tap water	I <sub>DS</sub> -V <sub>DS</sub> measurements  I <sub>DS</sub> -V <sub>GS</sub> measurements  R-time measurements	0.1 ppb (BP FET on SiO <sub>2</sub> )  0.01 ppb (Suspended BP FET)	0.01 – 100 ppb	<ul style="list-style-type: none"> <li>• The suspended device functions in subthreshold regime that has optimum gating effect, smaller low frequency noise, and larger sensing area.</li> <li>• The optimum sensitivity was exhibited in the subthreshold regime.</li> <li>• Sensor response rate of 3 s.</li> <li>• Response of suspended BP sensor is 2-3 times larger than the BP FET on SiO<sub>2</sub> sensor.</li> <li>• Good repeatability (resistance shift &lt; 5%).</li> <li>• Good stability (good shape after 3 days with I<sub>DS</sub> variation &lt; 5%).</li> <li>• Good selectivity.</li> </ul>
[36]	BP/Au NPs/DTT-FET	As(III) As(V)	Lake water	I <sub>DS</sub> -V <sub>DS</sub> measurements	1 nM (As(III) and As(V))	1 nM – 1μM	<ul style="list-style-type: none"> <li>• BP film works as the channel material. Au NPs and DTT function as the active site to attract As ions</li> </ul>

				$I_{DS}$ - $V_{GS}$ measurements			and also work as chemical passivation improving the stability of BP film.
				$I_{DS}$ -time measurements			<ul style="list-style-type: none"> <li>• Sensor response of 1-2 s.</li> <li>• Good selectivity.</li> </ul>
[37]	Flexible integrated BP sensor arrays	Hg(II) Cd(II) Pb(II) Na(I)	Spiked tap water (Cd)  Human sweat (Na)	$I_{DS}$ - $V_{DS}$ measurements  $I_{DS}$ -time measurements	10 ppb (Hg)	$1 - 10^8$ ppb (Hg)	<ul style="list-style-type: none"> <li>• First study of BP flexible sensor arrays functionalized with selective ionophore.</li> <li>• The sensor shows excellent mechanical flexibility (strain limits of 1%) and stability (bending 500 times).</li> <li>• Small strain change leading to an 175% sensitivity enhancement.</li> <li>• Multiplexed detection of Hg(II), Cd(II), Pb(II), Na(I) at trace levels on flexible PET substrate (1x1 cm).</li> <li>• Sensor response rate of 4 s.</li> <li>• Good selectivity.</li> </ul>
[38]	BP FET	Pb(II)	---	$I_{DS}$ - $V_{DS}$ measurements  $I_{DS}$ - $V_{GS}$ measurements  EIS	1 ppb	1-100 ppb	<ul style="list-style-type: none"> <li>• An <math>Al_2O_3</math> passivation layer was deposited onto the BP by ALD, then sputtered with AuNPs and functionalized with GSH.</li> <li>• Improved stability, and good reproducibility and selectivity.</li> </ul>

[39]	BP FET	Ag(I)	---	$I_{DS}$ - $V_{DS}$ measurements  $I_{DS}$ - $V_{GS}$ measurements  $I_{DS}$ -time measurements	0.01 ppb	---	<ul style="list-style-type: none"> <li>• The greatest contribution for sensing performance was from the double-layer capacitance change produced by Pb(II) ions at the BP/<math>Al_2O_3</math> interface at the low frequency region (~50 Hz).</li> <li>• BP-FET is suitable for Ag(I) detection due to the cation-<math>\pi</math> interactions between Ag(I) and BP.</li> <li>• Detection time for each sample is 60 s.</li> <li>• The thickness of the BP directly influences the device sensing performance. A BP with a thickness of ~ 10 nm for the FET device production was selected.</li> </ul>
[40]	Hb@IL-PDDA-BP/GCE	NaNO <sub>2</sub>	---	CA, CV	3.65 $\mu$ M	80 $\mu$ M-3.8 mM	<ul style="list-style-type: none"> <li>• IL-PDDA-BP nanocomposite prepared with a simple non-covalent method displayed great biocompatibility, good solubility, and improved electric conductivity.</li> <li>• IL-PDDA-BP nanocomposite was employed as a suitable matrix for Hb immobilization.</li> <li>• The introduction of IL and PDDA</li> </ul>

improves BP solubility, dispersity and stability.

- The developed Hb@IL-PDDA-BP biosensor exhibited fast direct electron transfer and very good catalytic performance toward nitrite reduction.

[41]	BP-PEDOT:PSS-Hb/CILE	TCA NaNO <sub>2</sub> H <sub>2</sub> O <sub>2</sub>	Medical facial peel solution Soak water of pickled vegetables 3% medical H <sub>2</sub> O <sub>2</sub>	CV	1 mM (TCA) 0.033 mM (NaNO <sub>2</sub> ) 0.67 mM (H <sub>2</sub> O <sub>2</sub> )	3.0 - 460 mM (TCA) 0.1 – 30 mM (NaNO <sub>2</sub> ) 2.0 – 18 mM (H <sub>2</sub> O <sub>2</sub> )	<ul style="list-style-type: none"> <li>• For the first time BP was employed to reach electron transfer of redox protein with PEDOT:PSS as protection film.</li> <li>• Hb was immobilized on the electrode and demonstrated the direct electrochemistry, displaying a pair of clearly defined redox peaks, which suggest the positive effect of BP on the electron transfer.</li> <li>• Shows excellent electrocatalytic effects on the reduction of TCA, NaNO<sub>2</sub> and H<sub>2</sub>O<sub>2</sub>.</li> <li>• Good stability (deviation &lt; 10% after 80 cycles).</li> <li>• Good storage stability (94.5% of its original response after 20 days).</li> </ul>
------	----------------------	---	--	----	---	--	--

[42]	Hb-pLL-BP/GCE	H <sub>2</sub> O <sub>2</sub> O <sub>2</sub>	---	CA, CV	---	10-700 $\mu$ M	<ul style="list-style-type: none"> <li>• pLL enhances the stability of BP and preserve its good conductivity.</li> <li>• Apart from the role of BP in the Hb electrocatalytic performance, it is also appropriate to keep Hb native structure and inherent bioactivity.</li> <li>• Good selectivity towards H<sub>2</sub>O<sub>2</sub>.</li> </ul>
[43]	BPQDs-ZnO/GCE	H <sub>2</sub> O <sub>2</sub>	Spiked tap water	CA, CV	2.5 $\mu$ M	5 $\mu$ M – 0.05 mM 0.5 – 10 mM	<ul style="list-style-type: none"> <li>• BP was dopped with ZnO NPs leading to a change in the shape of this ZnO NPs.</li> <li>• The electrochemical performance improvement would be due to the increase of the materials' conductivity as a result of combining BPQDs and ZnO.</li> <li>• BPQDs/ZnO nanocomposite displays synergetic effects on the H<sub>2</sub>O<sub>2</sub> oxidation.</li> <li>• Good reproducibility (10 electrodes, RSD= 2.5 %).</li> <li>• Long-term stability (90% of its original response after one week at 4°C).</li> <li>• Sensor response time less than 3</li> </ul>

s.

[44]	BP-PEDOT:PSS-hemin/Cl	TCA NaNO <sub>2</sub> H <sub>2</sub> O <sub>2</sub>	Medical facial peel solution (35% TCA)	CV	0.67 mM (TCA) 0.33 mM (NaNO <sub>2</sub> ) 1.33 mM (H <sub>2</sub> O <sub>2</sub> )	2 – 180 mM (TCA) 1 – 10.5 mM (NaNO <sub>2</sub> ) 4 – 35 mM (H <sub>2</sub> O <sub>2</sub> )	<ul style="list-style-type: none"> <li>• BP and PEDOT:PSS was employed for the immobilization of hemin on CILE</li> <li>• BP improves the electron transfer from hemin to electrode.</li> <li>• Shows excellent electrocatalytic performance for the reduction of TCA, NaNO<sub>2</sub> and H<sub>2</sub>O<sub>2</sub>.</li> <li>• Good stability (the current response decreases for 7.8% after 70 cycles).</li> <li>• Long-term stability (92.2% of the sensitivity after 15 days at 4°C).</li> </ul>
[45]	BP coated FTO	AHB	Serasub™ with AHB	CV	---	0.8 - 8.75 ppb	<ul style="list-style-type: none"> <li>• BP coated sensor was used for electrochemical test using Serasub solution and different concentrations of AHB.</li> <li>• BP has an excellent potential for its usefulness towards biomarkers sensing</li> </ul>
[46]	PG – BP/GCE	Bisphenol A	Drinking water bottle Urine	CV, DPV	0.0078 μM	0.43 – 55 μM	<ul style="list-style-type: none"> <li>• First work on PG-BP based electrochemical sensors.</li> <li>• PG-BP significantly increases the surface area of the sensor.</li> </ul>

[47]	HA/BP-Tyr organic phase interdigital electrode (BTOPI)	Bisphenol A	Aquaculture water	Amperometry	10 nM	0.05-1 $\mu$ M	<ul style="list-style-type: none"> <li>• Good reproducibility (5 electrodes, RSD= 2.7 %).</li> <li>• Long-term stability (96.3% of its original response after one week at 4°C).</li> <li>• Good selectivity towards bisphenol A.</li> </ul>
							<ul style="list-style-type: none"> <li>• First work on BP as an organic phase enzyme biosensing platform.</li> <li>• BP was modified with HA as an easy non-covalent passivation strategy.</li> <li>• The BP modified sensor without Tyr did not response to bisphenol A.</li> <li>• BTOPI exhibits better analytical performance than the same sensor without BP.</li> <li>• Long-term stability (65% of its original response after 180 days in chloroform at 4°C).</li> <li>• Good repeatability (8 successive measurements, RSD= 0.5%).</li> <li>• Good selectivity towards bisphenol A.</li> </ul>

[48]	BP/GCE	Ochratoxin A	Grape juice Beer samples	CV, DPV	0.18 $\mu\text{g}\cdot\text{ml}^{-1}$	0.3 – 10 $\mu\text{g}\cdot\text{ml}^{-1}$	<ul style="list-style-type: none"> <li>• BP nanosheets were functionalized with <math>\text{Ag}^+</math> in NMP solution.</li> <li>• Stronger antifouling and good electrocatalytic activity towards ochratoxin A oxidation.</li> <li>• Good sensor stability in water containing <math>\text{O}_2</math>.</li> <li>• Good repeatability (20 successive measurements, RSD= 1.62%).</li> <li>• Good reproducibility (6 electrodes, RSD= 3.37 %).</li> <li>• Good selectivity towards ochratoxin A.</li> </ul>
[49]	BP-Nf(IP)/GCE	Clenbuterol	Spiked bovine meat and serum	CV, DPV	3.7 nM	0.06 – 24 $\mu\text{M}$	<ul style="list-style-type: none"> <li>• Synergistic effect among the different components of the BP nanocomposite.</li> <li>• Good sensor stability in water containing <math>\text{O}_2</math>.</li> <li>• Good electrocatalytic activity for clenbuterol electrooxidation.</li> <li>• Good repeatability (30 successive measurements, RSD= 1.1%).</li> <li>• Good reproducibility (6 electrodes, RSD= 2 %).</li> </ul>

[50]	S-β-CD- PEDOTNPs/BP/GCE	Clenbuterol Ractopamine	Spiked beef, feed, and bovine serum samples	CV, DPV	0.14 μM (Clenbuterol)  0.12 μM (Ractopamine)	0.3 – 90 μM (Clenbuterol)  0.3 – 9.4 μM (Ractopamine)	<ul style="list-style-type: none"> <li>• Good selectivity towards clenbuterol.</li> <li>• Clenbuterol and ractopamine were simultaneously determined.</li> <li>• The covering of both PEDOTNPs and S-β-CD coating improves BP stability.</li> <li>• Synergistic effects of BP, S-β-CD and PEDOTNPs.</li> <li>• An antifouling strategy based on the application of continuous cyclic voltammetry cycles was used.</li> <li>• Good sensor stability in water containing O<sub>2</sub>.</li> <li>• Good repeatability (18 successive measurements, RSD= 2.3 and 2.0 % for clenbuterol and ractopamine, respectively).</li> <li>• Good reproducibility (7 electrodes, RSD= 2.8 and 2.0 % for clenbuterol and ractopamine, respectively).</li> </ul>
[51]	BP-Au NC - Ap/SPCE	Okadaic acid	Spiked mussel samples	DPV	8 pM	10 – 250 nM	<ul style="list-style-type: none"> <li>• A microfluidic based aptasensor was developed.</li> <li>• Several BP-Au NC layers were</li> </ul>

drop-casted on the SPCE surface and further functionalized by aptamer immobilization.

- BP was coupled with Au NP for improved electroconductivity.
- Average assay time of 30 min.
- The sensor did not exhibit any cross-reactivity with other food toxins.

[52]	BP-PEDOT:PSS/GCE	Rutin	Rutin tablet samples	CV, DPV	0.007 $\mu\text{M}$	0.02 – 15 $\mu\text{M}$ 15 – 80 $\mu\text{M}$	<ul style="list-style-type: none"> <li>• PEDOT:PSS showed excellent adhesive strength to avoid the leaking of BP nanosheet from the GCE surface.</li> <li>• BP-PEDOT:PSS demonstrated exceptional electrochemical conductivity.</li> <li>• Long-term stability (96.68 and 95.35% of its original oxidation and reduction currents, respectively, after one week at 4°C).</li> <li>• Good reproducibility (5 electrodes, RSD= 3.26 %).</li> <li>• Good repeatability (9 successive measurements, RSD= 1.78 and 1.50% for oxidation and reduction</li> </ul>
------	------------------	-------	----------------------	---------	---------------------	--	--

currents, respectively).

- Good selectivity towards rutin.

[53]	BP-FET	IgG	---	$I_{DS}$ - $V_{DS}$ measurements  $I_{DS}$ - $V_{GS}$ measurements  $I_{DS}$ -time measurements	~10 ppb	10 – 500 ppb	<ul style="list-style-type: none"> <li>• FET biosensor was manufactured by using few-layer BP nanosheets labeled with Au NPs-antibody conjugates.</li> <li>• BP nanosheet surface was passivated by an Al<sub>2</sub>O<sub>3</sub> dielectric layer for preserving BP from being oxidized in aqueous solutions.</li> <li>• The gating effect is the main sensing mechanism for the surface passivated BP biosensor.</li> <li>• Good stability: small changes in the sensor resistance (24%) and the on-off current ratio (5%), after 5 days under ambient conditions.</li> <li>• Good selectivity towards IgG.</li> <li>• Sensor response time on the order of seconds.</li> </ul>
[54]	BSA/Ab/Glu/Cys/Au NPs/Pg-BP/GCE	Leptin	Spiked human serum	SWV	0.036 pg ml <sup>-1</sup>	0.150 - 2500 pg ml <sup>-1</sup>	<ul style="list-style-type: none"> <li>• The immobilization approach of Au NPs and Cys self-assembled layer make the antigen more strongly immobilized on the electrode surface.</li> <li>• The effective surface area of PG-</li> </ul>

BP sensor is increased about 5 times as compared to bare GCE.

- Good repeatability (6 successive measurements, RSD= 6.27%).
- Long-term stability (92.32% of its original response after 7 days at 4°C).
- Good selectivity towards leptin.
- This immunosensor presents superior performance as compared with other electrochemical methods.

[55] BP - HMA - Au NPs - Ap/Au electrode      PCB77      Tap water      DPV      33 pg L<sup>-1</sup>      100 pg L<sup>-1</sup> – 10 μg L<sup>-1</sup>

- The passivation of BP with HMA in chloroform makes it possible to maintain its original form in aqueous solution for over a month.
- BP is doped with Au NPs to enable the binding to PCB77 aptamer.
- Its sensibility is about 3 times higher than that of the Au NPs-Ap/Au electrode.
- Long-term stability (90% of its original response after one week at 4°C).
- Good repeatability (8 successive

[56]	Ap-BP NSs/TH/Cu-MOF/GCE	MicroRNA (miR3123)	Spiked fresh human serum	SWV	0.3 pM	2 pM – 2 μM	<p>measurements, RSD &lt; 5%).</p> <ul style="list-style-type: none"> <li>• Good selectivity towards PCB77.</li> <li>• 2D MOF was prepared using PTTBA and Cu(NO<sub>3</sub>)<sub>2</sub> as precursors and TH as doping agent. BP NSs were then added to make BP NSs/TH/Cu-MOF complex.</li> <li>• The aptasensor were obtained by combining ferrocene-labeled single-strand DNA Ap with the complex.</li> <li>• Ap-BP NSs/TH/Cu-MOF/GCE works as a smart ratiometric electrochemical aptasensor.</li> <li>• Long-term stability (one week protected with and opaque cover and incubated at 4°C in a dark place).</li> <li>• Good repeatability (6 successive measurements, RSD &lt; 2.3%).</li> <li>• Good selectivity towards miR3123.</li> </ul>
[57]	Nf/BP NSs-G2-β-CD/GCE	Tryptophan enantiomers L-Trp and D-Trp	---	SWV	1.07 μM (L-Trp) 1.71 μM	0.01 – 1.00 mM	<ul style="list-style-type: none"> <li>• Nf worked as the protective film to immobilize BP NSs-G2-β-CD on the surface of the electrode.</li> <li>• The sensor confirms</li> </ul>

					(D-Trp)		<p>stereospecificity for Trp enantiomers due to the host-guest size matching assumption between G2-<math>\beta</math>-CD and amino acid enantiomers.</p> <ul style="list-style-type: none"> <li>• Good repeatability (6 successive measurements, RSD= 2.14 and 3.12% for L-Trp and D-Trp, respectively).</li> <li>• Good reproducibility (6 independent times, RSD= 4.06 and 3.38% for L-Trp and D-Trp, respectively).</li> <li>• Good selectivity towards Trp enantiomers.</li> </ul>
[58]	NH <sub>2</sub> -MWCNT-BP-Ag NPs/GCE	Uric acid Xanthine Hypoxanthine	Spiked bovine serum	CV, DPV	0.052 $\mu$ M (UA) 0.021 $\mu$ M (XT) 0.25 (HX)	0.1 - 800 $\mu$ M (UA) 0.5 - 680 $\mu$ M (XT) 0.7 - 320 $\mu$ M (HX)	<ul style="list-style-type: none"> <li>• NH<sub>2</sub>-MWCNT-BP-Ag NPs nanocomposite displays excellent electrocatalytic capacity and exceptional enzyme-like kinetic characteristics.</li> <li>• Ag NPs and NH<sub>2</sub>-MWCNT serve as a protective layer that prevented BP degradation under the conditions including water.</li> <li>• Good repeatability (25 successive measurements, RSD= 2.72, 2.69 and 2.24% for UA, XT and HX,</li> </ul>

respectively).

- Good reproducibility (7 electrodes, RSD= 2.03, 1.22 and 2.31% for UA, XT and HX, respectively).
- Long-term stability (> 90% of its original response after 15 days at 4°C).

[59]	PPy-BPQDs-MIPs/PEDOTNRs/GCE	Ascorbic acid	Spiked soft drink	DPV	0.0033 mM	0.01 – 4 mM	<ul style="list-style-type: none"><li>• BPQDs and ascorbic acid was self-assembled onto PEDOTNRs surface.</li><li>• MIP sensor was prepared by electrochemical polymerization, using PPy as functional monomer and ascorbic acid as template molecule.</li><li>• Good reproducibility (4 electrodes, 3 successive measurements in each electrode, RSD= 3.58 %).</li><li>• Long-term stability (93.4% of its original response after 10 days).</li><li>• Good selectivity towards ascorbic acid.</li></ul>
[60]	BPNSs/GCE	Ascorbic acid	Vitamin C tablet	DPV	0.3 nM	1–35 nM	<ul style="list-style-type: none"><li>• BPNSs were synthesized through liquid exfoliation method coupling with ultrasonication.</li></ul>

[61]	BP-Au NP-Ap/Au interdigital electrode	Malachite green	Aquaculture water	DPV	0.3 ng L <sup>-1</sup>	1 - 10 <sup>4</sup> ng L <sup>-1</sup>	<ul style="list-style-type: none"> <li>• Ascorbic acid response increased ~ 6 times and the oxidation potential was negatively shifted in comparison with the bare GCE.</li> <li>• Good repeatability (5 measurements, RSD= 4.5%).</li> <li>• Long-term stability (&lt;10% decrease of the response was obtained after one week at 4°C).</li> <li>• Ascorbic acid determination could be influenced by reagents with a very close oxidation peak.</li> </ul>
							<ul style="list-style-type: none"> <li>• L-cysteine is used for the first time for non-covalent coating on BP surface to protect it from degradation and oxidation.</li> <li>• BP works as a signal amplifier and aptamer acts as a recognition sector for malachite green selective detection.</li> <li>• L-cysteine – BP resists about 2 weeks in aqueous solution while without L-cysteine, BP is damaged within 12h.</li> <li>• Good repeatability (8 measurements, RSD= 5%).</li> <li>• Good selectivity towards</li> </ul>

malachite green.

[62]	Ab2/MB/Au@Fe <sub>3</sub> O <sub>4</sub> @COF-PSA/OVA/ Ab1/Au@BP/GCE	PSA	Spiked human serum	DPV	30 fg mL <sup>-1</sup>	10 <sup>-4</sup> - 10 ng mL <sup>-1</sup>	<ul style="list-style-type: none"><li>• First work on PSA determination using BP as substrate and magnetic COF as the nanoprobe for electrochemical signal generation and amplification.</li><li>• Au@BP was used as an immunosensing support to attach primary Ab and enhance electron transfer.</li><li>• Au NP-COF was utilized to immobilize the secondary Ab and ample electronic signals of MB.</li><li>• Long-term stability (&gt; 95.5% of its original response after 15 days at 4°C).</li><li>• Good reproducibility (6 electrodes, RSD= 2.03%).</li><li>• Good selectivity towards PSA.</li></ul>
[63]	BP@PDA-SCX8·FA/ GCE/Au	LNCaP cells	Spiked human serum	EIS	36 cells mL <sup>-1</sup>	200 – 10 <sup>5</sup> cells mL <sup>-1</sup>	<ul style="list-style-type: none"><li>• A cytosensor based on SCX8 and PDA - modified BP via host-guest recognition between SCX8 and FA was reported.</li><li>• The large BP surface area improves the BP@PDA nanocomposite preparation.</li></ul>

[64]	ECL probe/exosomes/ Ap/ILs/SiO <sub>2</sub> NUs/GCE	Exosomes	Spiked human serum	ECL	37 particle $\mu\text{L}^{-1}$	1.1x10 <sup>2</sup> – 1.1x10 <sup>7</sup> particle $\mu\text{L}^{-1}$	<ul style="list-style-type: none"> <li>• BP@PDA–SCX8·FA can recognize the FR and capture cancer cells by forming an SCX8–FA–FR sandwich-type conjugate.</li> <li>• The BP stability was enhanced by PDA polymerization.</li> <li>• Good selectivity towards cancer cells.</li> <li>• An ECL and photothermal dual-mode biosensor was developed.</li> <li>• ECL probe consists of MXenes-BPQDs@Ru(dcbpy)<sub>3</sub><sup>2+</sup>-PEI-Ab<sub>CD63</sub></li> <li>• SiO<sub>2</sub> Nus act as sensing platform providing numerous immobilization sites for Ap.</li> <li>• EpCAM protein could be recognized by the Ap and then capture exosomes.</li> <li>• Signal probe marked with Ab<sub>CD63</sub> could be identified by the exosomes modified on the electrode.</li> <li>• Good stability (ECL intensity is almost constant after 10 cyclic scans, RSD: 1.1%. For photothermal sensor, RSD: 2.1%</li> </ul>
------	--	----------	-----------------------	-----	--------------------------------	---	--

after 10 laser off/on).

- Good specificity between Ap and exosomes.

[65]	Lyz/BSAN/DNA/probe /GE	Lysozyme	Spiked human serum	ECL	0.029 pg mL <sup>-1</sup>	0.1 - 10 <sup>2</sup> pg mL <sup>-1</sup>	<ul style="list-style-type: none"><li>• BSAN was prepared by inserting BPQDs into poly(styrene/acrylamide) copolymer nanospheres.</li><li>• Firstly, mercapto group terminated Lyz Ap was attached on GE through S-Au bond as the probe.</li><li>• BSAN was linked with DNA through the amino group on polymer film, and then BSAN/DNA was immobilized onto the electrode via hybridizing with the probe.</li><li>• BSAN functions as coreactant to produce ECL with Ru(bpy)<sub>3</sub><sup>2+</sup>.</li><li>• Good stability (ECL intensity is almost constant after 9 cyclic scans, RSD: 0.56%).</li><li>• Long-term stability 90% of its original response after 3 weeks stored in refrigerator).</li><li>• Good reproducibility (6</li></ul>
------	------------------------	----------	--------------------	-----	---------------------------	---	--

[66]	Pb(II) Ap labeled Ag/AgCl nanocubes /capture DNA and MCH decorated BP nanoflakes/GCE	Pb(II)	Spiked tap water Spiked lake water	ECL	0.27 pM	0.5 pM – 5 nM	<p>electrodes, RSD= 1.2%).</p> <ul style="list-style-type: none"> <li>• Good specificity to lysozyme.</li> <li>• An ECL assay procedure was conceived on the basis of Pb(II) induced ECL-RET between 2D BP nanoflakes and Ag/AgCl nanocubes.</li> <li>• BP nanoflakes were used as new anodic ECL luminophores without any coreactants.</li> <li>• Good stability (ECL intensity is almost constant after 10 cyclic scans).</li> <li>• Good reproducibility (intra-assay with five parallel tests, RSD: 4.3%; and inter-assay with 5 electrodes, RSD: 5.1%).</li> <li>• Good selectivity towards Pb(II).</li> </ul>
------	--	--------	---------------------------------------	-----	---------	---------------	---

---

Ab: antibody; Ab1 and Ab2: PSA antibody; AHB: alfa-hydroxybutyrate; ALD: atomic layer deposition; Ap: aptamer; BPQDs: black phosphorus quantum dots; BSA: bovine serum albumin; BSAN: BPQDs-St-AAm nanospheres; BTOPI: HA/BP-Tyr organic phase interdigital electrode; CA: chronoamperometry; CILE: carbon ionic liquid electrode; COF: covalent organic frameworks; CV: cyclic voltammetry; Cys: cysteamine; DTT: dithiothreitol; DPV: differential pulse voltammetry; ECL: electrochemiluminescence; ECL-RET: electrochemiluminescence resonance energy transfer; EIS: electrochemical impedance spectroscopy; FA: folic acid; FET: field-effect transistor; FR: folic receptor; FTO: fluorine doped tin oxide; G2-  $\beta$ -CD: 6-O- $\alpha$ -maltosyl- $\beta$ -cyclodextrin; GCE: glassy carbon electrode; GE: gold electrode; Glu: glutaraldehyde; GSH: glutathione; HA: hexamethyldiamine; Hb: hemoglobin; HMA:

hexamethylenediamine; HX: hypoxanthine;  $I_{DS}$ : drain – source current; IgG: immunoglobulin G; IL: [bmim][BF<sub>4</sub>] (ionic liquid); ILs: 1-carboxymethyl-3-methylimidazolium chloride (ionic liquid); Lyz: lysozyme; MB: methylene blue; MCH: 6-mercaptohexanol; MIP: molecularly imprinted polymer; MOF: metal-organic frameworks; MWCNT: multiwall carbon nanotubes; Nf: nafion; Nf(IP): nafion treated with isopropanol; NMP: N-methyl pyrrolidone; NPs: nanoparticles; NSs: nanosheets; OVA: ovalbumin; PCB77: 3,3',4,4'-polychlorinated biphenyl; PDA: polydopamine; PDDA: poly(diallyldimethylammonium chloride); PEDOT:PSS: poly(3,4-ethylenedioxythiophene) -poly(styrenesulfonate); PEDOTNRs: poly(3,4-ethylenedioxythiophene) nanorods; PEI: polyethylenimine; PG: porous graphene; pLL: poly-L-lysine; PPy: polypyrrole; PSA: prostate specific antigen; PTTBA: 4,4',4'',4'''-(porphine-5,10,15,20-tetracyl)tetrakis benzoic acid; R-time: resistance-time; RSD: relative standard deviation; S- $\beta$ -CD: mono(6-mercapto-6-deoxy)- $\beta$ -cyclodextrin; SCX8: p-sulfonated calix[8]arene; SiO<sub>2</sub> NUs: SiO<sub>2</sub> nanourchin; SPCE: screen-printed carbon electrode; SWV: square wave voltammetry; TCA: trichloroacetic acid; TH: thionine; Trp: tryptophan; Tyr: tyrosinase; UA: uric acid;  $V_{DS}$ : drain - source voltage;  $V_{GS}$ : gate – source voltage; XT: xanthine.

**Table 3.** Antimonene, bismuthene, and arsenene -based sensors for electrochemical sensing applications.

Ref.	2D material	Analyte	Sensor type	Sample	Technique	Detection limit	Linear range	Additional Information
[68]	Antimonene	Phenol	Antimonene/Tyr/ Glu/GCE  Arsenene/Tyr/Glu /GCE  Bismuthene/Tyr/ Glu/GCE  Phosphorene/Tyr /Glu/GCE	Spiked tap water	CV, CA	255 nM	7.5 – 27.5 nM  500 – 2500 nM	<ul style="list-style-type: none"> <li>• First biosensor approach built using exfoliated pnictogens beyond phosphorene.</li> <li>• The enhanced performance of the antimonene-based phenol biosensor can be assigned to the highest degree of exfoliation and downsizing, the lowest ratio of oxidation of its surface, and the biocompatibility.</li> <li>• Antimonene/Tyr/Glu/GCE reveals excellent analytical performance with high sensitivity, good repeatability (RSD= 17.68%, 10 different concentration, each repeated 3 times), good selectivity and specificity towards phenol.</li> </ul>
[69]	Antimonene	BRCA1 gene	DNA probe/ antimonene/ AuSPE	Clinical DNA samples of the BRCA1 gene	DPV	28.3 pg $\mu\text{L}^{-1}$	Up to 20.0 ng $\mu\text{L}^{-1}$	<ul style="list-style-type: none"> <li>• First work that uses 2D antimonene for SPE modification as DNA sensing platform.</li> </ul>

[70]	Antimonene	H <sub>2</sub> O <sub>2</sub>	Cat/AMQDs-GCE	Ovarian cancer serum	CV Amperometry	4.4 μM	50 – 300 μM	<ul style="list-style-type: none"> <li>• FL-antimonene interacts strongly with DNA.</li> <li>• This biosensor discriminates between clinical samples from healthy (BRCA gene) and diseased (mutated gene) patients.</li> <li>• Good reproducibility (5 electrodes, error &lt; 5%).</li> <li>• Long-term stability (98% of its original response after one month).</li> </ul>
								<ul style="list-style-type: none"> <li>• First work that uses AMQDs in sensing applications.</li> <li>• Catalase enzyme was immobilized onto AMQDs and has electrocatalytic activity towards H<sub>2</sub>O<sub>2</sub> reduction.</li> <li>• The sensor is stable up to 30 cycles. Recovery of 95-103.4%.</li> <li>• Good selectivity in presence of glucose, ascorbic acid, leucine and dopamine.</li> <li>• H<sub>2</sub>O<sub>2</sub> concentration increases with higher levels of CA125.</li> </ul>

[20]	Antimonene Bismuthene Arsenene	Ascorbic acid	Antimonene/GCE Bismuthene/GCE Arsenene/GCE	---	CV, LSV	---	---	<ul style="list-style-type: none"> <li>• First work that uses 2D pnictogens as sensing platforms for electrochemical applications.</li> <li>• It is proved that aqueous shear exfoliation can be applied to get Sb, As and Bi exfoliated nanosheets.</li> <li>• The electrochemical performance is assessed in terms of electron transfer, inherent electrochemistry, and sensing applications.</li> <li>• The shear exfoliated pnictogens show improved catalytic properties compared to the bulk pnictogens.</li> </ul>
[71]	Antimonene Bismuthene Arsenene	Glucose	pnictogen <sub>SE</sub> - Au@AgNR/GCE	---	CV, DPV	3.5 pM	50 pM – 555.550 nM	<ul style="list-style-type: none"> <li>• Shear exfoliated pnictogen nanosheets were mixed with Au@AgNRs as a new electrode material for the preparation of an enzyme-less glucose sensor.</li> <li>• Sb<sub>SE</sub>-Au@AgNR, Bi<sub>SE</sub>-Au@AgNR and As<sub>SE</sub>-Au@AgNR composites were synthesized.</li> <li>• Only As<sub>SE</sub>-Au@AgNR composite provides clear CV signals in the</li> </ul>

presence of glucose, showing exceptional electrocatalytic ability towards its oxidation.

- The lack of response of  $\text{Sb}_{\text{SE}}-\text{Au}@Ag\text{NR}$  and  $\text{Bi}_{\text{SE}}-\text{Au}@Ag\text{NR}$  could be attributed to the absence of gold in these composites.
- Acceptable sensor reproducibility (RSD < 15%).
- A LPE procedure to prepare FL arsenene assisted by sonication and without any additional surfactant is reported.
- An application of arsenene for construction of vapor sensor based on EIS is demonstrated.
- The 2D As nanosheets selectivity toward MeOH and acetone depends on the frequency used.
- Long-term stability (97 and 94% of their original response after three weeks at the ambient air for MeOH and acetone sensors, respectively)

[72]	Arsenene	MeOH and acetone vapors	Arsenene/ Au Interdigitated electrode	---	EIS	---	---
------	----------	-------------------------	---------------------------------------	-----	-----	-----	-----

[6]	Arsenene (black and grey)	MeOH, EtOH, Et <sub>2</sub> O, isopropanol, acetone, acetonitrile, air	Arsenene/ Au interdigitated electrode	---	EIS	---	---	<ul style="list-style-type: none"> <li>• The arsenene materials are stable for 8 days in ambient conditions.</li> <li>• The application of arsenic samples as impedimetric sensors for volatile organic compounds was investigated.</li> <li>• Grey arsenene shows sensitivity towards MeOH and EtOH, while black arsenene shows sensitivity towards MeOH, EtOH, isopropanol, acetone and acetonitrile.</li> <li>• Good stability of the tested impedimetric sensors.</li> </ul>
[73]	Bismuthene	Pb(II), Cd(II)	Bismuthene/Gra/GCE	Tap water	SWASV	0.3 ppb	1-30 ppb	<ul style="list-style-type: none"> <li>• Reports for the first time the implementation of bismuthene (combined with graphene) for the ASV determination of Pb(II) and Cd(II) ions.</li> <li>• Three different ratios of bismuthene and graphene were tested (1:10, 1:5, 1:2,5 w/w) revealing that the 1:5 w/w dispersion endows the greatest sensitivity.</li> <li>• Good repeatability of bismuthene/Gra/GCE (15</li> </ul>

successive measurements, RSD= 3.4 and 6.8% for Pb(II) and Cd(II), respectively).

- Good reproducibility of bismuthene/Gra/GCE (10 electrodes, RSD< 3.3 and 1.4% for Pb(II) and Cd(II), respectively).
- The bismuthene/Gra/GCE sensor shows excellent working stability allowing more than 40 measurements keeping 95% of the original signal.

[74]	Bismuthene	Pb(II), Cd(II)	Bismuthene/SPCE	Estuarine water	DPASV	0.06 ppb (Pb) 0.07 ppb (Cd)	0.2-25 ppb	<ul style="list-style-type: none"> <li>• First application of pure bismuthene drop-casted onto an SPCE for the ASV determination of Pb(II) and Cd(II) ions.</li> <li>• Improved detection limits as compared to other Bi-modified electrodes.</li> <li>• Good repeatability of bismuthene/SPCE (5 successive measurements, RSD= 3.0 and 4.2% for Pb(II) and Cd(II), respectively).</li> <li>• Good reproducibility of bismuthene/SPCE (3 electrodes, RSD= 1.2 and 1.0% for Pb(II) and Cd(II), respectively).</li> </ul>
------	------------	----------------	-----------------	-----------------	-------	--------------------------------	------------	---

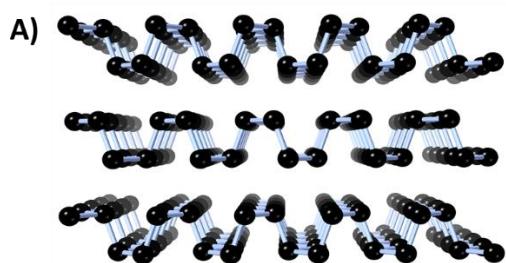
- Long-term stability (stored at least one week under inert atmosphere without signals of stability loss).

---

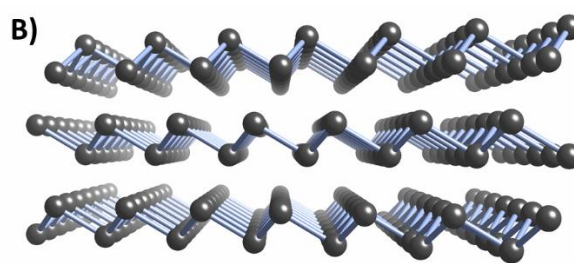
AMQDs: antimonene quantum dots; ASV: anodic stripping voltammetry; Au@AgNR: gold@silver nanorod; AuSPE: gold screen printed electrode; CA: chronoamperometry; CV: cyclic voltammetry; DPV: differential pulse voltammetry; DPVASV: differential pulse anodic stripping voltammetry; EIS: electrochemical impedance spectroscopy; EtOH: ethanol; Et<sub>2</sub>O: diethyl ether; FL: few-layered; GCE: glassy carbon electrode; Gra: graphene; Glu: glutaraldehyde; LSV: linear sweep voltammetry; LPE: liquid-phase exfoliation; MeOH: methanol; SPE: screen-printed electrode; SPE: screen-printed carbon electrode; SWASV: square-wave anodic stripping voltammetry; Tyr: tyrosinase.

**Figure 1**

Orthorhombic (A) and rhombohedral (B) crystal structures of 2D layered pnictogens. The first structure is the thermodynamically stable form of synthetic black-phosphorus and arsenic with puckered layers, while the rhombohedral structure is the most common for naturally occurring grey-arsenic, antimony, and bismuth with parallel buckled layers.



orthorhombic, black,  $\alpha$ -phase



rhombohedral, grey,  $\beta$ -phase

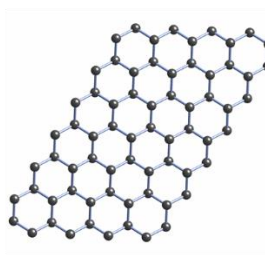
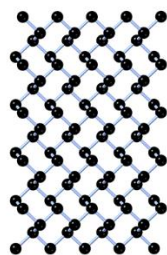


## Figure 2

A) Images of multi-cm size orthorhombic BP crystal specimen grown by vapor transport method inside glass ampule, produced at the Sofer's Lab, University of Chemistry and Technology, Prague. B) Scheme with "top-down" methods for production of 2D layered materials by ultrasonication, shear force methods and electrochemical exfoliation. Reproduced from ref. [8], with permission. C) High-resolution XPS spectra and peaks deconvolutions of the Sb 3d core level region (overlapping with O 1s) for layered grey Sb. Reproduced from ref. [10], with permission. D) HR-TEM/EDS analysis of bismuthene. The magenta colors in the index demonstrates distribution mapping of bismuth element. Reproduced from ref. [14], with permission. E) AFM of antimonene sheet fabricated by mechanical exfoliation is highly stable under atmospheric conditions over periods of months and even when immersed in water. Reproduced from ref. [15], with permission. F) Single-point Raman spectra of arsenene measured at different thicknesses according to the topographic AFM image (inset scale bar is equal to 500 nm) of the small area. Reproduced from ref. [16], with permission. G) Raman spectra of G1) black arsenic and G2) grey arsenic with labelled their respective phonon modes (LL 532 nm, 50 mW) with applied power of 5 mW and 50x magnification objective. Reproduced from ref. [6], with permission. H) Contrasts in the electrochemical activity of basal-plane and edge-plane BP towards biosensing applications using as analytes ascorbic acid (H1) and dopamine (H2) at 0.01 M level in 0.05 M PBS and scan rate  $100\text{mV s}^{-1}$ . Reproduced from ref. [17], with permission.

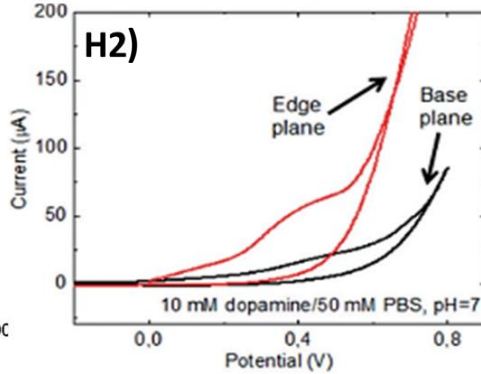
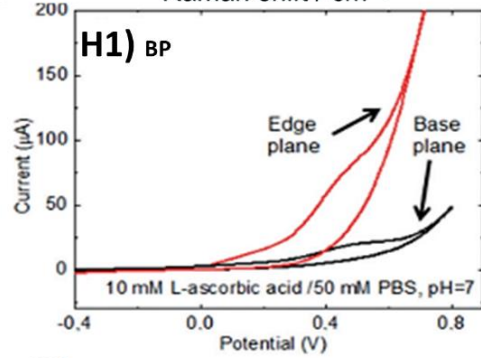
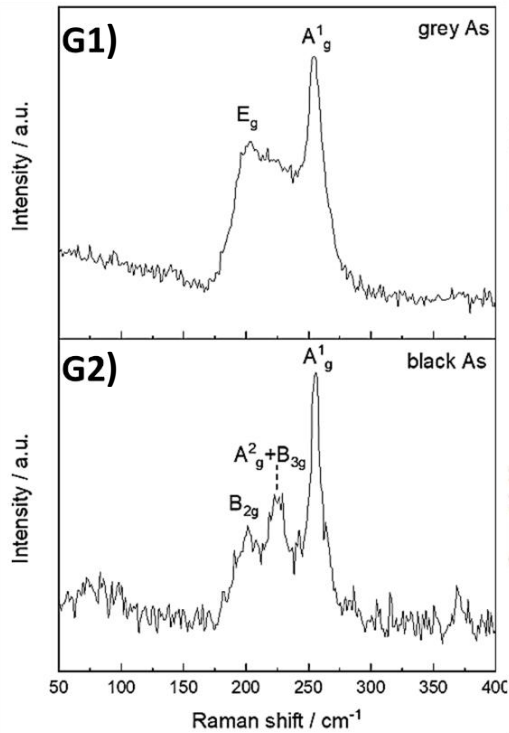
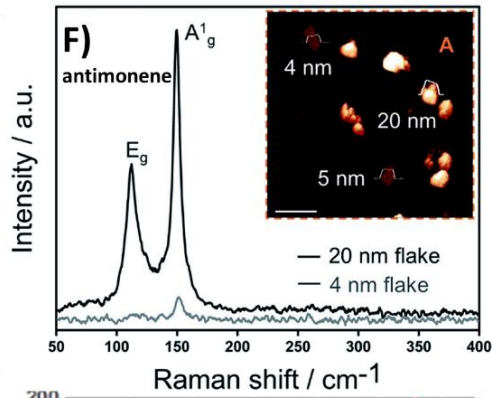
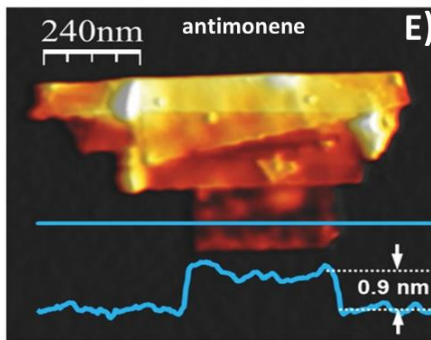
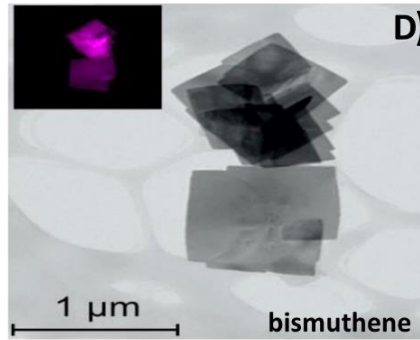
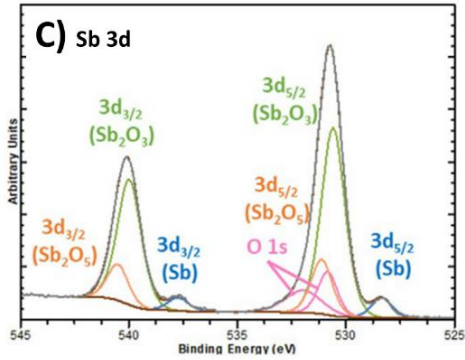


**Figure 3**

Scheme of the water adsorption model of a BP-based QCM humidity sensor. Reproduced from ref. [22] with permission.

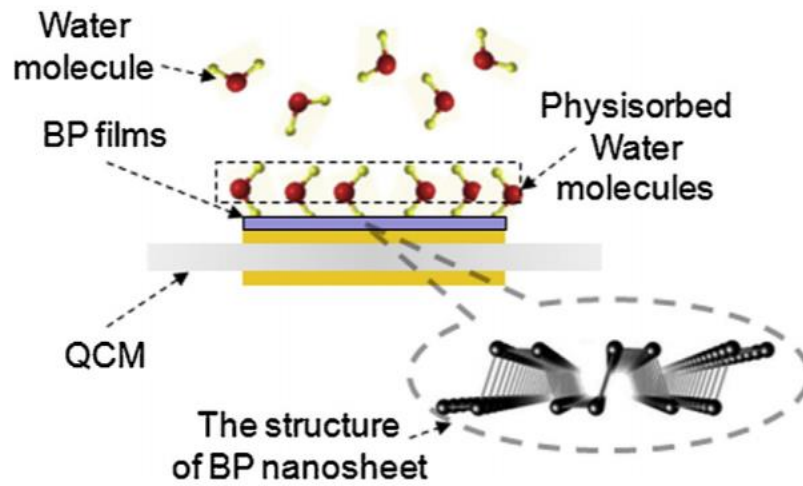


**Figure 4**

Fabrication of Pt-functionalized BP hydrogen sensors *via* dry transfer. BP flakes were transferred to the Ti/Au pre-patterned SiO<sub>2</sub>/p-Si substrate and coated with Pt NPs prior to the application of the PMMA layer. Reproduced from ref. [34] with permission.

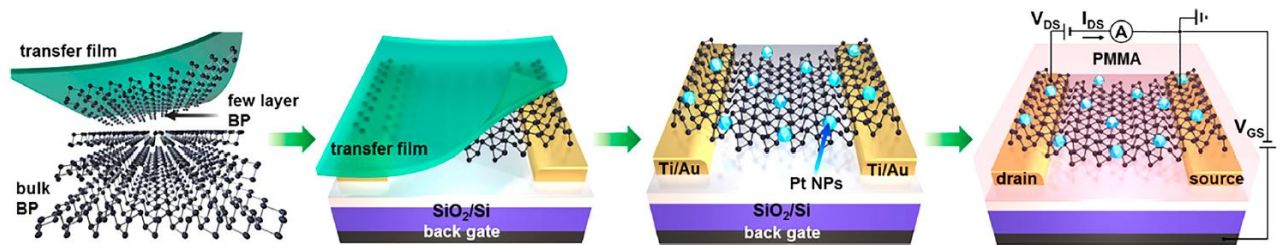


**Figure 5**

A) Schematic of the BP/Au NPs/DTT sensing platform for the As ion detection; B) Reaction between the DTT and As(III) ion in the detection process. Electronic characteristics and real-time sensing performance of the FET sensor platform: C)  $I_{ds}$ - $V_{gs}$  curve with the bias voltage  $V_{ds}$  ranging from  $-40$  to  $40$  V ( $V_{ds} = 0.1$  V); D)  $I_{ds}$ - $V_{ds}$  curve with the  $V_{ds} = -1$  V  $\sim$   $1$  V ( $V_{gs} = 0$  V); E) Real-time detection of As(III) in water ( $V_{ds} = 0.1$  V,  $V_{gs} = 0$  V) with the BP/Au NPs/DTT platform, for concentrations ranging from  $1$  nM to  $1$   $\mu$ M. Adapted from ref. [36] with permission.

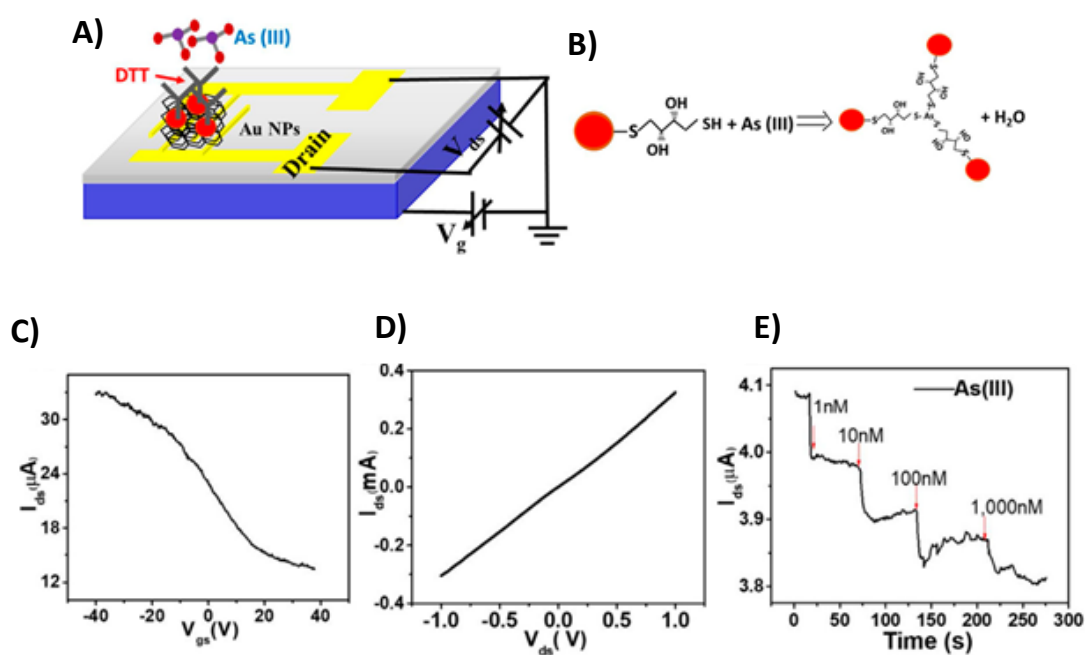


**Figure 6**

Schematic representation of an ECL biosensor based on BP quantum dots for the detection of lysozyme. Reproduced from ref. [65] with permission.

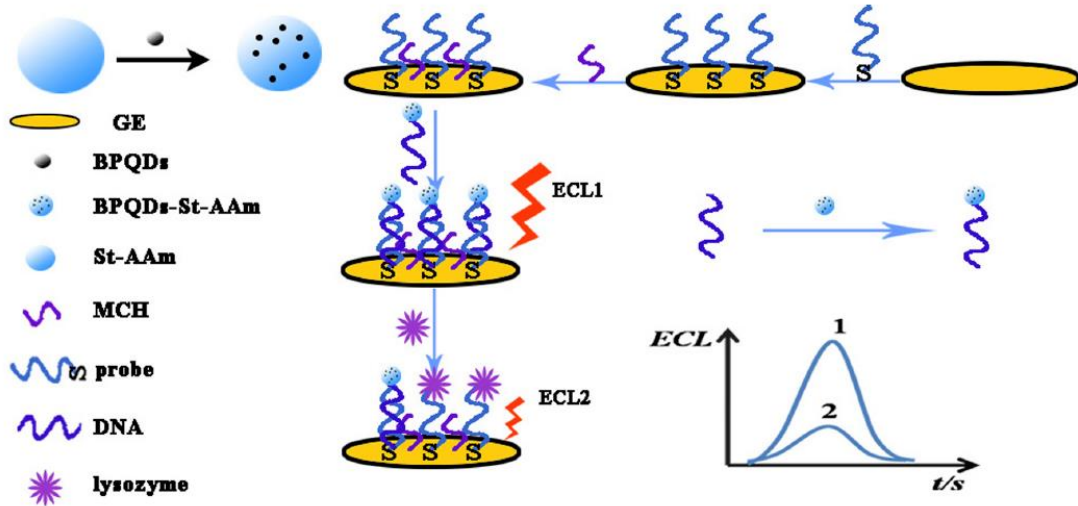


**Figure 7**

A) Amperometric response of the BPQDs@ZnO/GCE to successive additions of  $\text{H}_2\text{O}_2$  in  $0.1 \text{ mol L}^{-1}$  PBS. The inset shows a close look of rectangular region with the  $\text{H}_2\text{O}_2$  concentration from  $5 \mu\text{mol L}^{-1}$  to  $0.05 \text{ mmol L}^{-1}$ . B) and C) are linear calibration curves of amperometric responses as functions of the concentration of  $\text{H}_2\text{O}_2$ . D) Detection of  $\text{H}_2\text{O}_2$  in tap water samples. Reproduced from ref. [43] with permission.

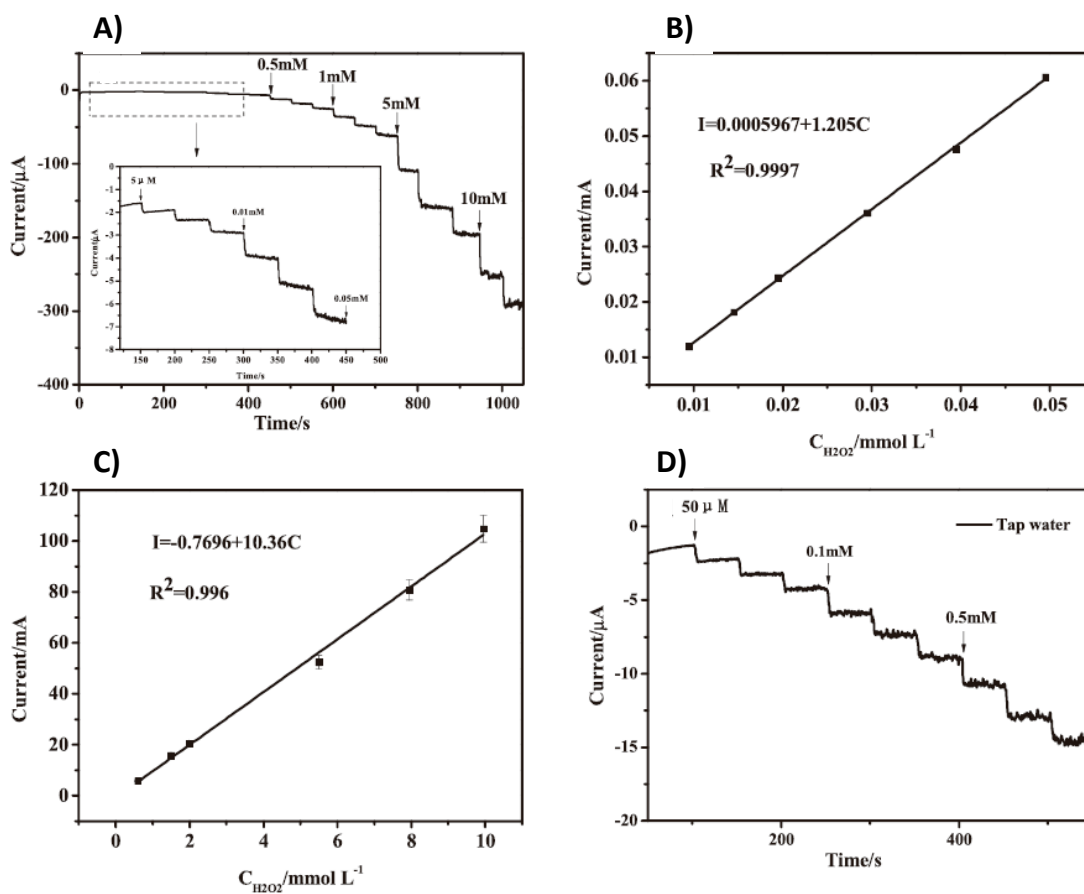


**Figure 8**

A) DPVs of OTA with different concentrations at BP/GCE. OTA concentrations from a to h of 0.3, 0.5, 0.7, 1, 3, 5, 7 and 10 mg/mL, respectively. B) The linear relationship between peak currents and OTA concentrations. Reproduced from ref. [48] with permission.

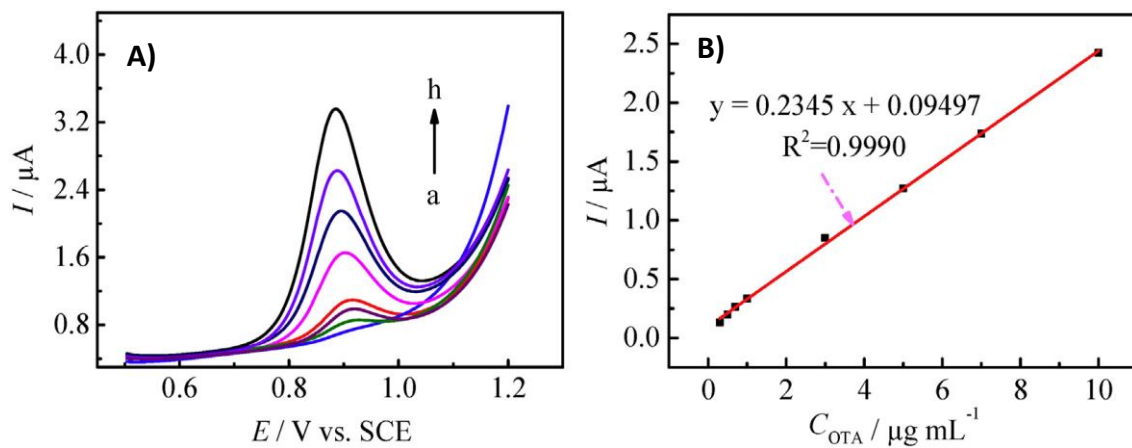


**Figure 9**

Response of impedimetric sensors based on grey and black arsenic to various VOCs plotted as Bode diagrams. Reproduced from ref. [6] (Open access).

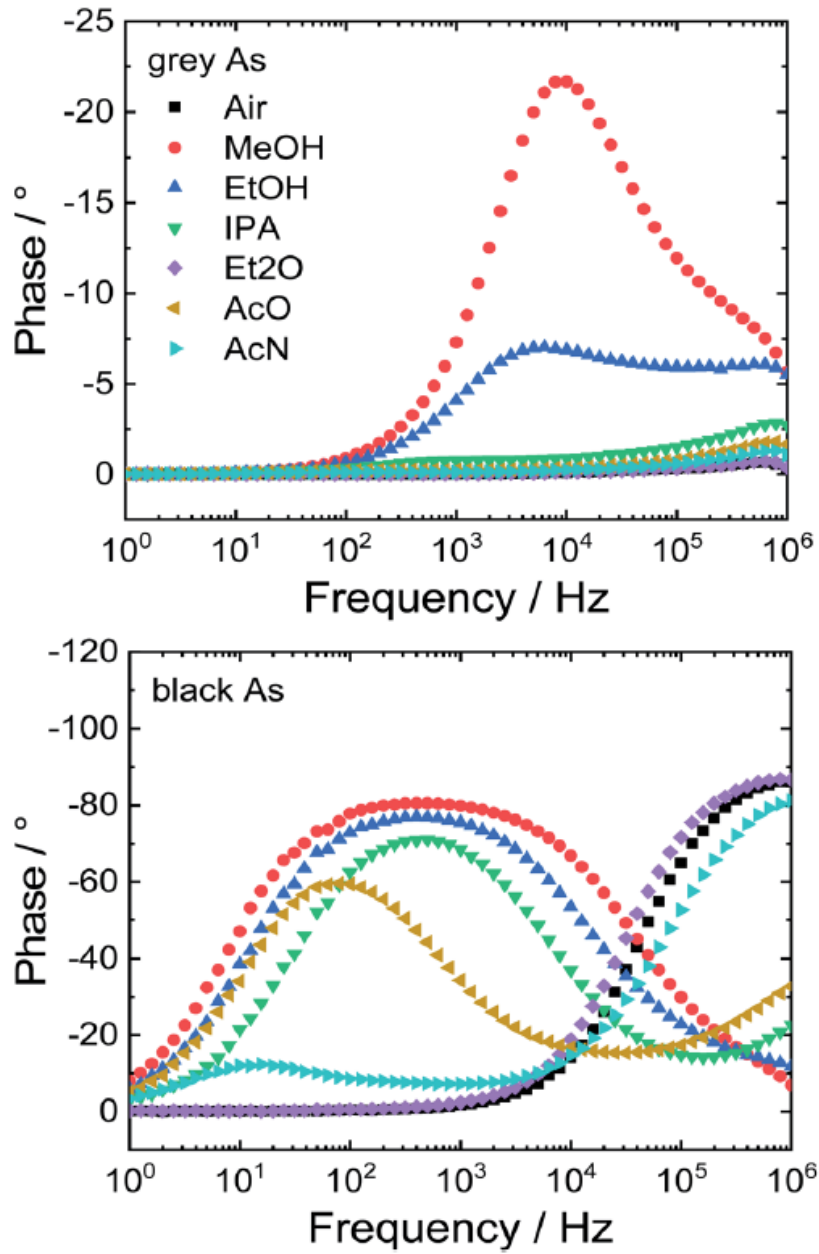


### Figure 10

A) DP stripping voltammograms of  $25 \mu\text{g L}^{-1}$  Pb(II) and Cd(II) recorded on Bare-SPCE (dashed line), BiNP-SPCE (dotted-dashed line), Bi<sub>sp</sub> SPE (thin line) and 2D Bi<sub>exf</sub>-SPCE (thick line) using a deposition potential of  $-1.3 \text{ V}$  during 120 s at pH 4.5; B) DP stripping measurements in a certified estuarine water sample recorded with 2D Bi<sub>exf</sub>-SPCE using a deposition potential of  $-1.3 \text{ V}$  in  $0.1 \text{ mol L}^{-1}$  acetate buffer during 120 s at pH 4.5. The original signal of the sample is denoted with a thick line; Inset: Standard addition representation for the determination of Pb(II) and Cd(II) concentration. Reproduced from ref. [74] with permission.

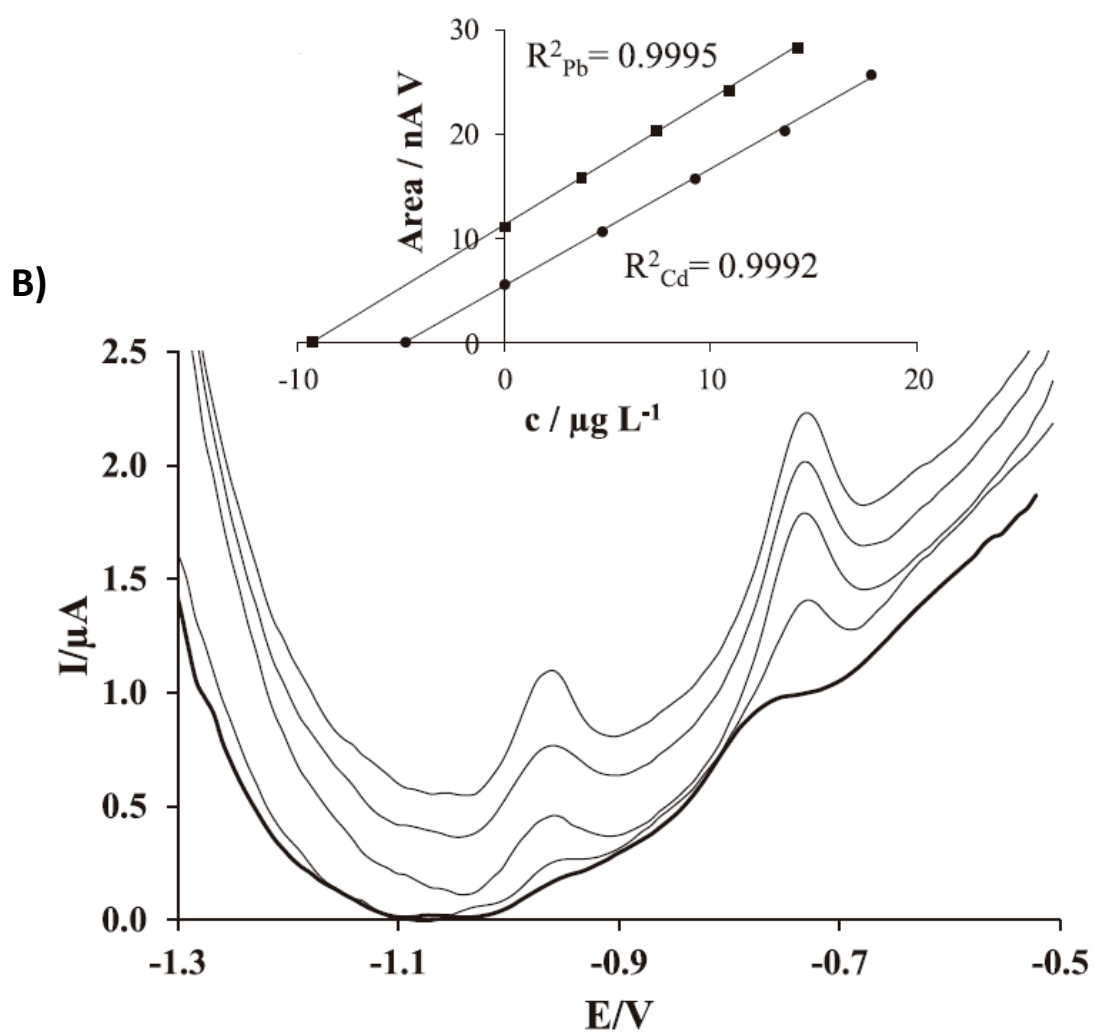
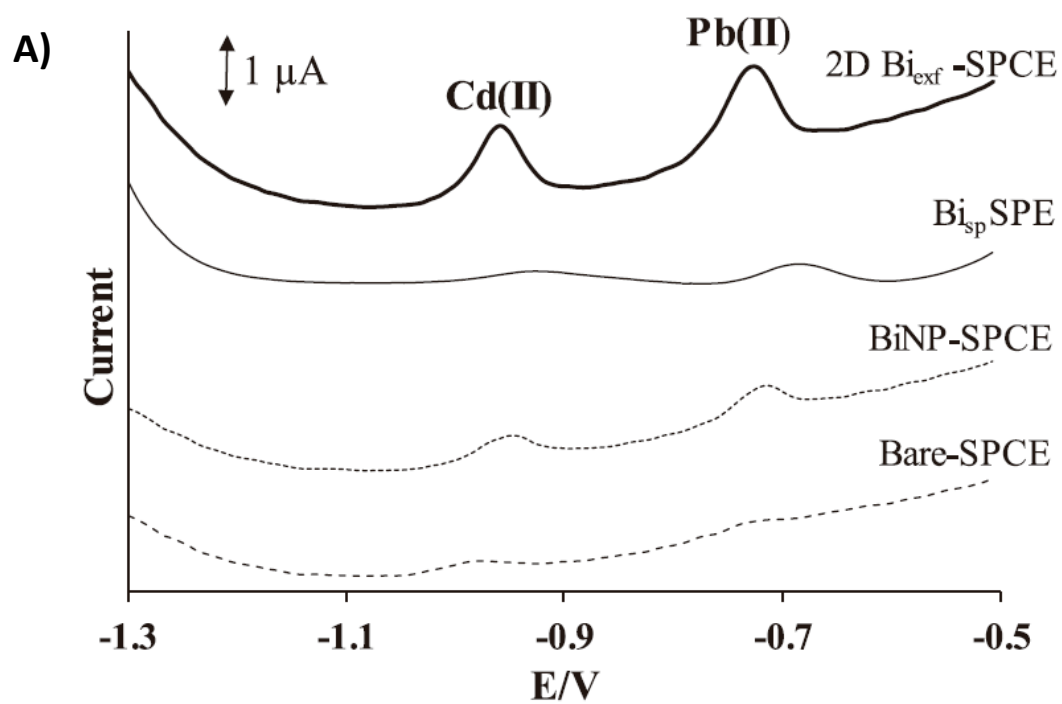


**Figure 11**

A) Shear exfoliated pnictogens using kitchen blender. B) Biosensor preparation using layer-by-layer drop-casted pnictogen nanosheets, tyrosinase (Tyr), and glutaraldehyde (Glu) onto a glassy carbon (GC) electrode. C) Chemical mechanism of phenol detection by biosensor based on exfoliated pnictogen and Tyr. Reproduced from ref. [68] with permission.

